Strong and reliable synaptic communication between pyramidal neurons in adult human cerebral cortex

Sarah Hunt, Yoni Leibner, Eline J Mertens, Natalí Barros-Zulaica, Lida Kanari, Tim S Heistek, Mahesh M Karnani, Romy Aardse, René Wilbers, Djai B Heyer, et al.

OXFORD

Cerebral Cortex, 2023, **33**, 2857–2878
https://doi.org/10.1093/cercor/bhac246
Advance access publication date 8 July 2022
Original Article

Strong and reliable synaptic communication between pyramidal neurons in adult human cerebral cortex

Sarah Hunt[1,†], Yoni Leibner[2,†], Eline J. Mertens[1], Natalí Barros-Zulaica[3], Lida Kanari[3], Tim S. Heistek[1], Mahesh M. Karnani[1], Romy Aardse[1], René Wilbers[1], Djai B. Heyer[1], Natalia A. Goriounova[1], Matthijs B. Verhoog[1,‡], Guilherme Testa-Silva[1,§], Joshua Obermayer[1], Tamara Versluis[1], Ruth Benavides-Piccione[4], Philip de Witt-Hamer[5], Sander Idema[5], David P. Noske[5], Johannes C. Baayen[5], Ed S. Lein[6], Javier DeFelipe[4], Henry Markram[3], Huibert D. Mansvelder[1], Felix Schürmann[3], Idan Segev[2], Christiaan P.J. de Kock[1,*]

[1]Department of Integrative Neurophysiology, Center for Neurogenomics and Cognitive Research, Vrije Universiteit Amsterdam, 1081 HV Amsterdam, the Netherlands,
[2]Department of Neurobiology and Edmond and Lily Safra Center for Brain Sciences, The Hebrew University of Jerusalem, 9190501 Jerusalem, Israel,
[3]Blue Brain Project, Ecole polytechnique fédérale de Lausanne, Campus Biotech, Geneva 1202, Switzerland,
[4]Laboratorio Cajal de Circuitos Corticales, Universidad Politécnica de Madrid and Instituto Cajal (CSIC), Pozuelo de Alarcón, Madrid 28223, Spain,
[5]Neurosurgery Department, Amsterdam Universitair Medische Centra, location VUmc, 1081 HV Amsterdam, the Netherlands,
[6]Allen Institute for Brain Science, Seattle, WA 98109, USA
*Corresponding author: Email: ckock@falw.vu.nl
[†]Sarah Hunt and Yoni Leibner have equal contribution.
[‡]Present address: Department of Human Biology, Neuroscience Institute, University of Cape Town, South Africa.
[§]Present address: Institute of Molecular and Clinical Ophthalmology Basel, 4031 Basel, Switzerland.

Synaptic transmission constitutes the primary mode of communication between neurons. It is extensively studied in rodent but not human neocortex. We characterized synaptic transmission between pyramidal neurons in layers 2 and 3 using neurosurgically resected human middle temporal gyrus (MTG, Brodmann area 21), which is part of the distributed language circuitry. We find that local connectivity is comparable with mouse layer 2/3 connections in the anatomical homologue (temporal association area), but synaptic connections in human are 3-fold stronger and more reliable (0% vs 25% failure rates, respectively). We developed a theoretical approach to quantify properties of spinous synapses showing that synaptic conductance and voltage change in human dendritic spines are 3–4-folds larger compared with mouse, leading to significant NMDA receptor activation in human unitary connections. This model prediction was validated experimentally by showing that NMDA receptor activation increases the amplitude and prolongs decay of unitary excitatory postsynaptic potentials in human but not in mouse connections. Since NMDA-dependent recurrent excitation facilitates persistent activity (supporting working memory), our data uncovers cortical microcircuit properties in human that may contribute to language processing in MTG.

Key words: synaptic transmission; cortex; L2/L3; human brain; NMDA receptor.

Introduction

From subcellular structure and function, to neuronal microcircuits, and through to cognitive brain networks, the cross-scale analyses of the human cerebral cortex are essential to understand its organizational and functional principles. At the subcellular level, organizational principles have been investigated by anatomical reconstructions (Jacobs et al. 2001; Benavides-Piccione et al. 2002), transcriptional profiling of surgical resection samples (Berg et al. 2021; Kalmbach et al. 2021), and post-mortem brain tissue (Hodge et al. 2019; Bakken et al. 2021), whereas macroscale measures were obtained in living human subjects through whole-brain electrophysiology and imaging (Varela et al. 2001; McDaniel 2005; Assaf et al. 2020; Douw et al. 2021). At the microcircuit resolution however, details on human single neuron and synaptic function are only starting to be uncovered (Beaulieu-Laroche et al. 2018; Seeman et al. 2018; Gidon et al. 2020). The data sparsity at the microcircuit level has led to a gap in the cross-scale understanding of human brain function in both health and disease.

Acute slices from surgically resected brain tissue of the human cortex offer a unique opportunity to study microcircuit properties of the human brain at subcellular scale. These ex-vivo tissue samples frequently originate from middle temporal gyrus (MTG; Brodmann area 21) and are part of the distributed semantic (Binder et al. 2009) and language-related processing streams (Hickok and Poeppel 2007; Heyer et al. 2022). These mesoscale networks require associative processing, which is facilitated

Received: March 8, 2022. **Revised:** May 25, 2022. **Accepted:** May 26, 2022

by human-specific genetic programs that drove cortical expansion of supragranular layers and increased cortical–cortical connectivity (Buckner and Krienen 2013). Also within temporal cortex, pyramidal neurons are the principle building blocks and are responsible for the main excitatory output both between cortical regions and to subcortical areas, which ultimately drive cognitive behavior. Understanding synaptic communication between these neurons may aid to our understanding of human cortical function (Molnar et al. 2008; Testa-Silva et al. 2014; Seeman et al. 2018; Campagnola et al. 2022). Yet, the bulk of our knowledge on L2/3 pyramidal microcircuits in cerebral cortex arises from rodent studies (Qi et al. 2020). Although broad characteristics are conserved between species, evidence is rapidly accumulating that we cannot indiscriminately apply the organizational and functional principles extracted from rodents to human neurons (Beaulieu-Laroche et al. 2018; Gidon et al. 2020; Berg et al. 2021).

In terms of morphology, human pyramidal neurons in temporal cortex are on average 3-fold larger in dendritic size (Mohan et al. 2015) and contain a higher spine density (Benavides-Piccione et al. 2002) compared with rodent. Consequently, human pyramidal neurons have a higher total spine count, which may translate to either more contact points per connection, an increase in the number of synaptic partners per neuron, or both. Physiologically, human neurons have distinct membrane properties and ion channel distribution (Kalmbach et al. 2018) allowing, together with their morphological differences, local dendritic compartmentalization, and nonlinear information processing (Eyal et al. 2014; Gidon et al. 2020), which may affect processing of local connections. Furthermore, excitatory synapses of human MTG pyramidal neurons typically show an increased size of presynaptic active zones, postsynaptic densities, and vesicle pools (Benavides-Piccione et al. 2002; Molnar et al. 2016; Yakoubi et al. 2019); the functional consequences of these anatomical adaptations on pyramidal-to-pyramidal synaptic transmission however are not yet known.

Pyramidal-to-pyramidal connections have recently been studied in human cerebral cortex; these are more frequently observed than in mouse V1 (Seeman et al. 2018) and are capable of more efficient information transfer (Testa-Silva et al. 2014). The strength, reliability, and wiring properties of these individual connections were not fully characterized and, in light of distinct neuronal properties between species, are important to investigate. Specifically, given that the anatomical evidence suggests that both the availability to receive inputs (Benavides-Piccione et al. 2002; Mohan et al. 2015), and the potential for neurotransmitter release and binding (Benavides-Piccione et al. 2002; Molnar et al. 2016; Yakoubi et al. 2019) may be increased in human, we reasoned that pyramidal-to-pyramidal connections could be stronger, more frequent and contain more contact points per connection. This may ultimately lead to a microcircuit that supports persistent activity and/or working memory, which could underlie language processing (Wang 2001; Hickok and Poeppel 2007; Binder et al. 2009). Due to the extended dendrites in human cerebral cortex, and potentially enhanced voltage attenuation and filtering (Beaulieu-Laroche et al. 2018; Kalmbach et al. 2018; Gidon et al. 2020), it is key to understand the functional implications of the extensive dendritic trees in human pyramidal cells and determine whether there are compensatory mechanisms in human synaptic connections, such as an increase in synaptic conductance and reliability, as compared with adult rodent (in comparable regions and experimental conditions).

Indeed, comprehensive understanding of the transcriptional diversity of the building blocks (i.e. neurons) of the human brain, their wiring rules, connection properties, and information processing in human microcircuits are crucial towards reliable and predictive modeling studies from which novel and effective therapies for neurological disorders may emerge (Beutel et al. 2020). Towards this goal, we performed multi-patch recordings from clusters of up to 4 pyramidal neurons in L2/L3 of ex-vivo slices, combined with 3D neuron reconstruction and identification of location of putative L2/3–L2/3 synapses in both human and mouse temporal cortex. Aided by detailed modeling and a novel cable-theoretical approach, we quantitatively characterize the properties of L2/L3 human synapses demonstrating their enhanced strength and reliability, and discuss the implications of our results for cortical microcircuit properties and function in the human brain.

Materials and methods

Human tissue

All procedures were performed with the approval of the Medical Ethical Committee of the Vrije Universiteit Medical Centre, and in accordance with Dutch license procedures and the Declaration of Helsinki. Written informed consent was provided by all subjects for data and tissue use for scientific research. All data were anonymized.

We obtained human neocortical brain tissue (originating from middle Temporal Gyrus, MTG, Brodmann area 21, 2–6-cm posterior with respect to the temporal pole, Fig. 1a) that was removed as part of surgical treatment of the subject in order to gain access to a disease focus in deeper brain structures. Tissue obtained for this study came from 16 patients (7 females, 9 males; age range: 18–69 years) treated for mesial temporal sclerosis, tumor removal, low grade hippocampal lesion, cavernoma, or another unspecified temporal lobe pathology (Supplemental Table S1). The resected neocortical tissue was not part of epileptic focus or tumor location and displayed no overt structural or functional abnormalities in preoperative MRI investigation, electrophysiological whole-cell recordings, or microscopic investigation of stained tissue.

Human slice preparation

Resected neocortical tissue from the temporal cortex (Brodmann area 21, 2–6-cm posterior with respect to the temporal pole, Fig. 1a) was transported and sliced in an oxygenated ice-cold choline-based solution (in mM: 110 choline chloride, 26 $NaHCO_3$, 10 D-glucose, 11.6 sodium ascorbate, 7 $MgCl_2$, 3.1 sodium pyruvate, 2.5 KCl, 1.25 NaH_2PO_4, and 0.5 $CaCl_2$). Slice preparation commenced at most 15 min after tissue resection. Pia was removed from the tissue block using fine forceps and the pia-white matter (WM) axis was identified. The tissue block was glued on the slicing platform such that the slice plane was as parallel to direction of apical dendrites as possible and 350-μm-thick brain slices were prepared using a Thermo scientific slicer (Microm HM 650 V) or a Leica VT1200 vibratome in ice-cold choline-based solution. Human cortical slices were transferred to a holding chamber with artificial cerebrospinal fluid (aCSF; in mM: 125 NaCl, 3 KCl, 1.2 NaH_2PO_4, 1 $MgSO_4$, 2 $CaCl_2$, 26 $NaHCO_3$, and 10 glucose) for 30 min at 34°C. Slices were then incubated for recovery at room temperature for at least 30 min before starting recordings. Human pyramidal connections have previously been studied using 1.3-mM $CaCl_2$ (Seeman et al. 2018; Campagnola et al. 2022) to avoid triggering complex polysynaptic events (Molnar et al. 2008). Here, we used 2-mM $CaCl_2$ for better comparison with the majority of rodent connectivity studies and observed few polysynaptic events. Only monosynaptic connections with short latency responses were included in the present study.

Mouse slice preparation

All experiments were carried out in accordance with the animal welfare guidelines and approval of the animal ethical committee of the VU Amsterdam, the Netherlands. Adult male and female wild-type C57BL/6J mice (6–10-week old, $n = 21$) were anesthetized using Euthasol (4-mg pentobarbital sodium in 0.2 mL of a 0.9% sodium chloride solution, intraperitoneal injection) and transcardially perfused with 10 mL of an oxygenated ice-cold choline-based solution. Mice were then decapitated and the brain was quickly removed and placed in oxygenated choline solution. Coronal 350-μm-thick brain slices were then made from temporal association area (−1.4 to −2.4 mm posterior, +4.8-mm lateral to Bregma) as described for human slice preparation.

Electrophysiology

Slices were visualized on an upright microscope (model BX51WI, Olympus), and whole-cell patch-clamp recordings were made using a Multiclamp 700B (Molecular Devices). Data were filtered at 4 kHz and sampled at 10 kHz, and acquired using pClamp 10 (Molecular Devices). Whole-cell recordings were made simultaneously from clusters of up to 4 pyramidal neurons at a time from layers 2 and 3 of human temporal cortex and layer 2/3 of mouse temporal association cortex (TeA). Neurons selected for inclusion in cluster recording were located within 100 μm of each other (x-plane) and typically between 40 and 120 μm from the surface of the slice (z-plane). Neurons within a cluster were thus located approximately at the same cortical depth (relative to the pial surface) and thus within the same cortical layer. Slices were continuously perfused with oxygenated aCSF heated to 34°C and recording electrodes (3–6 MΩ; borosilicate glass capillaries, Harvard Apparatus) were filled with a K-gluconate-based internal solution (in mM: K-gluconate 115, HEPES 10, KCl 4, Mg-ATP 4, K-Phosphocreatine 10, GTP 0.3, EGTA 0.2, and biocytin 5 mg/mL, pH 7.2 with KOH, and osmolarity 295 mOsm/kg). No corrections were made for liquid junction potentials (calculated to be 14 mV and measured experimentally to be 12 mV). To probe for connections during simultaneous recordings, all neurons in the cluster were held in current-clamp mode (at ∼ −70 mV) and 1 neuron at a time was injected with a short train of 4 current pulses (2 ms, 2 nA, and 20 Hz) to evoke action potentials. Meanwhile, membrane potential from the 1 to 3 other neurons in the cluster were recorded for response detection. This protocol was repeated up to 50 times, averaged for analysis and the same protocol was conducted on all other neurons in the cluster. Once a response was observed, we then ran further current-clamp protocols with AP trains between 5 and 40 Hz, and in a subset with the postsynaptic neuron in voltage clamp (held at −70 mV) for further analysis. Synaptic features were extracted from the first pulse in the train. All connections that occurred between 2 pyramidal neurons consisted of a depolarization of the postsynaptic membrane potential in current-clamp and were therefore considered to be excitatory (in these experimental conditions, connections that occurred between a presynaptic interneuron and postsynaptic pyramidal neuron resulted in a hyperpolarization of the postsynaptic membrane). Finally, on occasion we observed multiple connections within a cluster, in this case each connection was treated as an independent observation.

Immunohistochemistry

Following electrophysiological recordings, human and mouse slices were fixed in 4% paraformaldehyde (in phosphate buffer) and recorded cells were recovered with chromogen 3,3-diaminobenzidine (DAB) tetrahydrochloride using the avidin–biotin–peroxidase method (Horikawa and Armstrong 1988) and annotated to layer borders revealed by DAPI staining to confirm L2/L3 identity of recorded neurons. DAB staining partially dehydrates tissue (Egger et al. 2008) and results in ±63% shrinkage in the z-plane (Egger et al. 2008; Mohan et al. 2015). Slices were mounted on slides without further dehydration steps and embedded in mowiol (Clariant GmbH, Frankfurt am Main, Germany). Only neurons with uniform biocytin staining and without apparent slicing artifacts were digitally reconstructed using Neurolucida software. Digital reconstructions were not corrected for

shrinkage (Microbrightfield, Williston, VT, United States), using a ×100 oil objective (1.4 N.A.). After reconstruction, morphologies were verified for accurate reconstruction in x/y/z planes, dendritic diameter, and continuity of dendrites. Finally, reconstructions were checked using an overlay in Adobe Illustrator between the Neurolucida reconstruction and Z-stack projection image from Surveyor Software (Chromaphor, Oberhausen, Germany). The DAPI staining was used to determine the distance from pia to the border between L3 and L4, which was in the current sample on average at $1{,}388 \pm 237$ μm from pia. The border measurement in combination with distance measurement between pia and recorded neurons allowed verification that all recordings included in this study were performed in L2/L3. Morphological subcategorization of recovered neurons was performed as previously described (Deitcher et al. 2017; Kanari et al. 2018) and only neurons with visibly complete dendritic structures were included; cells with major truncations due to slicing procedure were excluded. In the case that axons were successfully recovered, putative synapses were identified using a ×100 oil objective (1.4 N.A.) and were defined as a cross-over between axon and dendrite that occurred in the same focal plane (Feldmeyer et al. 2002), but see (Holler et al. 2021). The axon involved in each putative synapse was then traced back to its originating neuron; only putative synapses that could be reliably linked back to the presynaptic neuron, as identified by electrophysiological recordings and recording microdrive coordinates, were counted in the putative synapse analysis.

Our final dataset on EPSP features in human MTG includes $n = 32$ connections. Of the 32 recorded pairs, we had 4 reciprocal connections, 2 cases where a single presynaptic neuron contacted 2 different postsynaptic neurons and one case with 2 different presynaptic neurons contacting the same postsynaptic neuron. Based on these numbers, histology should result in 53 biocytin-labeled pyramids.

We recovered 42 and were able to confirm in all these cases the pyramidal identity of the recorded neurons. Of those 42 recoveries, we found 22 morphologies with incomplete apical dendrites. This is due to increased difficulty to orient resected human issue with respect to the coronal plane during slicing (relative to mouse tissue processing). We found 6 morphologies with weak biocytin signal relative to background and recovered 14 morphologies without major apical dendrite truncations (Fig. 3 and Supplemental Table S4). Neurons that were digitally reconstructed for computational simulations are illustrated in Supplemental Figs. S8 (human) and 9 (mouse).

Intracellular injections in fixed tissue

Human fixed brain tissue was used in a previous study obtained at autopsy (Benavides-Piccione et al. 2013). Mouse tissue sample was obtained from a C57BL/6 adult (8-week old) male mice that was perfused and fixed as in Benavides-Piccione et al. (2020). Vibratome sections (300 μm in the human; 200 μm in the mouse) of the temporal association cortex of the human (Brodmann's area 20) and mouse (TeA) were obtained in the coronal plane. Human and mouse sections were prelabeled with 4,6-diamidino-2-phenylindole (DAPI; Sigma, St Louis, MO), and a continuous current was used to inject individual cells with Lucifer yellow (LY; 8% in 0.1 M Tris buffer, pH 7.4) in the temporal association cortex of human and mouse (Supplemental Fig. S7). LY was applied to each injected cell by continuous current until the distal tips of each cell fluoresced brightly, indicating that the dendrites were completely filled and ensuring that the fluorescence did not diminish at a distance from the soma. Following the intracellular injections, the sections were immunostained for LY using rabbit antisera against LY (1:400,000; generated at the Cajal Institute) diluted in stock solution (2% bovine serum albumin, 1% Triton X-100, and 5% sucrose in PB). The sections were then incubated in biotinylated donkey anti-rabbit IgG (1:100; Amersham, Buckinghamshire, United Kingdom) and streptavidin-conjugated Alexa fluor 488 (1:1,000; Molecular Probes, Eugene, OR, United States). Finally, the sections were washed and mounted in 50% glycerol in PB. See Elston et al. (2001) and Benavides-Piccione et al. (2013) for further details of the cell injection methodology.

Computational modeling

Extracting the release probability using the Tsodyks–Markram model

We used a previously described Tsodyks–Markram-based model (Tsodyks and Markram 1997; Maass et al. 2002; Barros-Zulaica et al. 2019), to extract utilization of synaptic efficacy (U parameter) from a subset of human and mouse connections ($n_{human} = 21$ connections, $n_{mouse} = 21$ connections). This parameter represents the percentage of resources used at the presynaptic level when an action potential occurs (Markram et al. 1998). This model allowed us to follow the synaptic dynamics of a connection that can predict the sequence of EPSP amplitudes produced by a train of spikes (Tsodyks and Markram 1997). We used voltage traces where trains of current pulses (2 ms and 2 nA) were applied to evoke presynaptic action potentials: either the previously described probing protocol (4 presynaptic action potentials at 20 Hz) or a train of 7 presynaptic action potentials (5–40 Hz) followed by one recovery pulse at a 500-ms delay. For each connection, we first measured the peak EPSP amplitude of the average voltage trace. To accurately perform computations of the peaks we next deconvolved the average voltage trace (Richardson and Silberberg 2008) and then normalized traces to their maximum peak value. The peak values were then introduced into a genetic algorithm (Goldberg and Holland 1988), using BluePyOpt to extract, and optimize U within the range of 0–1.0 (Maass et al. 2002; Van Geit et al. 2016).

Extracting passive cable properties

We reconstructed detailed passive compartmental and cable models for 4 L2/3 human neurons and 4 mouse L2/3 neurons that were both morphological reconstructed and biophysically characterized. For each modeled neuron, we fitted the experimental input resistance (R_N) measured following a 1-s-long hyperpolarizing current pulse and extracted the neuron's membrane time constant, τ_0, and the first equalizing time constant, τ_1, through "peeling" the somatic voltage transients following brief current pulses (Fig. 4b and c, and see Rall 1969a, 1969b). This enabled us to estimate the electrotonic length of the dendritic tree, $L_{peel} = \sqrt{\pi/(\tau_0/\tau_1 - 1)}$, see Rall 1969a, 1969b. Fixing the specific axial resistivity, R_a, at 250 Ω*cm as in Eyal et al. (2018) and using the gradient-based algorithm implemented in *NEURON*, we obtained a unique value for the specific membrane resistivity, R_m (Ω*cm^2) per modeled cell that fitted its experimental R_N value (Fig. 4b). Having R_m and τ_0 provided the specific membrane capacitance, $C_m = \tau_0/R_m$ (in F/cm^2, Fig. 4c). In order to account for the presence of dendritic spines, we used the "*F*-factor" method to incorporate the spine membrane area into the modeled dendrites. In each dendritic branch we computed *F*, where *F* = ((spine area + dendritic area)/dendritic area), see Eyal et al. (2018). Consequently, we multiplying the estimated value for C_m (obtained for the morphology without spines) by *F* and divided R_m value by *F*. In addition, proximal dendritic structures typically lack spines. Consequently, the *F*-factor was set to 1.0 for the initial 60 μm of both apical and basal dendrites. The total membrane area of the spines for a given modeled neuron was calculated based on spine parameters provided in Supplemental Table S2 and specific densities of spines per dendritic compartment was taken from (Benavides-Piccione et al. 2002, 2013). Note that, due to tapering of dendritic branches and heterogeneous dendritic diameter, the F-factor differs for individual dendritic compartments. This resulted in a median $F_{human} = 2.13$ (range 1.75–2.44) and $F_{mouse} = 1.54$ (range 1.41–1.79), for human and mouse models, respectively.

Fitting somatic EPSPs based on dendritic location of the synapses

Having detailed passive models for the postsynaptic L2/3 neurons, we added a spine model at the dendritic locations where synaptic contacts were experimentally found. Spine morphological parameters are summarized in Supplemental Table S2. Spines were modeled as an isopotential head (RC) compartment, connected to the dendritic base by an axial resistance (representing the spine-neck resistance, R_{neck}, see Supplemental Fig. S8 and Segev and Rall (1988)). R_{neck} was computed as

$$R_{neck} = \frac{4 l_{neck} R_a}{\pi (d_{neck})^2} \quad (1)$$

where l_{neck} is the length of the spine neck; d_{neck} is the diameter of the spine neck and R_a is the specific axial (cytoplasm) resistance (in Ω*cm) whose value ranges between 150 and 250 in Ω*cm. Neck diameter was based on the anatomical range of spine-neck diameters for human and mouse spines which varied in our simulations between 0.09 and 0.25 μm for human and 0.07–0.25 for mouse, respectively (Tonnesen et al. 2014). The upper limit here for spine diameter (0.25 μm) resulted in a value of 68.8 MΩ for human spines and 37.2 MΩ for the mouse, when assuming axial resistivity of 250 Ω*cm at the spine neck. We also assumed smaller spine-neck diameters in our simulations (resulting in R_{neck} values of 200 and 500 MΩ) in order to examine to what degree our results depend on spine dimensions (Fig. 4i and j), especially since the spine-neck diameter can be below optical resolution of our confocal microscopy (Benavides-Piccione et al. 2002).

Unless otherwise stated (see Fig. 4 R_{neck} and Supplemental Fig. S10 for variable g_{AMPA}), for any given modeled neuron, the synaptic parameters (see below) at all modeled spines were identical (as in Supplemental Table S2). To fit the experimentally measured somatic EPSPs, given the synaptic locations and numbers of contacts, we used the genetic algorithm developed under BluePyOpt (Van Geit et al. 2016) to find the AMPA- and NMDA-conductances that resulted with the minimal mean square error between the modeled somatic EPSP and the respective experimental EPSP (Fig. 4). The resultant conductances and kinetics are summarized in Supplemental Table S3. Passive parameters for the spines were similar to that of the respective modeled neuron.

The synaptic current I_{syn} impinging on the spine head membrane was modeled as,

$$I_{syn} = g_{syn}(t, V) * (V - E_{syn}) \quad (2)$$

where g_{syn} is the transient synaptic conductance change and E_{syn} is the reversal potential for the synaptic current. E_{syn} was set to 0 mV for both the AMPAR and the NMDAR mediated currents.

For both AMPA and the NMDA components, the synaptic conductance was modeled using 2-state kinetic synaptic models—with rise time (τ_{rise}) and decay time (τ_{decay}) constants,

$$g_{syn}(t, V) = B * g_{max} * N * \left(\exp\left(-t/\tau_{decay}\right) - \exp\left(-t/\tau_{rise}\right)\right) \quad (3)$$

Here, g_{max} is the maximal synaptic conductance and *N* is a normalization factor given by,

$$N = \frac{1}{\exp\left(-\tau_{rise}/\tau_{decay}\right) - \exp\left(-t_{peak}/\tau_{rise}\right)} \quad (4)$$

t_{peak} (time of the peak conductance) is,

$$t_{peak} = \frac{\tau_{rise} * \tau_{decay}}{\tau_{decay} - \tau_{rise}} * \log\left(\frac{\tau_{decay}}{\tau_{rise}}\right) \quad (5)$$

The voltage dependence of the NMDA conductance is implemented by the factor B as in (Jahr and Stevens 1990),

$$B = \frac{1}{1 + \exp(-\gamma * V) * [Mg^{2+}] * n} \quad (6)$$

$\left[Mg^{2+}\right]$ was fixed at 1 mM, γ = 0.076 (1/mV), n = 0.27 (1/mM) and B = 1 for the AMPA-mediated component.

In Supplemental Fig. S10, we further explored our model predictions for the case where the number of putative synapses per connection was reduced to 40% (and then rounded up to the closest integer) as well as for the case where AMPA-conductance was permitted to vary among the synaptic contacts/connection.

Synapto-centric cable models

Although the properties of individual spines and their respective synapses where identical for all synaptic contacts in a given postsynaptic cell, our models predicted a large variability in the size of the EPSP at the spine head membrane for the various spines/synapses per cell. In order to understand the origin of this large variability, we developed a novel approach that enables one to appreciate the impact of the dendritic tree as viewed from the perspective of the spinous dendritic synapses. Towards this end, we characterized the conductance load imposed by the dendritic tree on a particular spine by computing both the sum of the dendritic membrane area as a function of the physical distance from the modeled spine (Fig. 4f–h, blue insets), as well as the "equivalent cable" for the whole neuron, as viewed from the spine head membrane. The equivalent diameter, d_{eq}, of this equivalent cable is,

$$d_{eq}(X) = \left(\sum_j (d_j(X))^{3/2}\right)^{2/3} \quad (7)$$

where X is the cable (electrotonic) distance from the spine (in units of the electrotonic length, λ) and $d_j(X)$ is the diameter of the ith dendrite at the distance X from the spine Fig. 4f–h) red/brown insets, see Rall (1959) and Burke et al. (1988).

These "synapto-centric equivalent cables," as seen from the spine perspective, provide a graphical intuition (as well as an analytical understanding, see below) for the degree of electrotonic decoupling of a given dendritic spine from the dendritic conductance load imposed on the spine. The large variability in these equivalent cables, for different spines belonging to the same postsynaptic neuron, explains the large variability in the amplitude of the local EPSP in different spines albeit receiving identical synaptic input. The shape of these "synapto-centric equivalent cables", in association with the dendritic location of the respective spines could be intuitively grasped by observing the electrotonic dendrogram in Fig. 4d.

The synapto-centric equivalent cables could be further approximated (simplified) by an equivalent cylinder (with uniform diameter), in which the spine is connected at one (sealed) end and the other (right) end is "leaky," with R_{leak} resistance connecting this end to the ground. R_{leak} represents the large sink imposed by the dendritic tree on the spiny-synapse. For each spine and its respective dendritic cylinder, R_{leak} is the input resistance at the junction point between the red and brown cables in Fig. 4f–h, in the absence of the red cable. For dendritic spines connected to such equivalent cylinders, a mathematical derivation for the voltage as well the input resistance at the spine head is provided by Equations (8) and (9) below. We note that these equations, which are valid for the steady-state case are also valid for the time-integral of the EPSP (proportional to the synaptic charge) at the spine head (Rinzel and Rall 1974). Indeed, Supplemental Fig. S7 shows that Equations (8) and (9) are excellent predictors of the synaptic charge and voltage at the spine head membrane, even in the presence of dendritic nonlinearity due to the NMDA current). This is for the case where the injected current at the spine head, I_{spine} in Equation (8), is replaced by the time-integral of $(I_{AMPA}(t) + I_{NMDA}(t)$ comprising the synaptic current injected at the spine head membrane.

From Ohms law, see also Rall (1974),

$$V_{spine} = I_{spine} * R_{head} \cong I_{spine} * (R_{neck} + R_{base}) \quad (8)$$

where V_{spine} is the (synaptic) potential at the spine head membrane, I_{spine} is the synaptic current injected to the spine head; R_{head} is the input resistance at the spine head, R_{neck} and R_{base} are the spine-neck resistance and the input resistance at the spine base, respectively.

For the equivalent cylindrical cable model with spine connected at its left end as shown in Supplemental Fig. S8 (Rall and Agmon-Snir 2001), R_{base} is

$$R_{base} = R_\infty \left(\frac{(R_{Leak}/R_\infty)\cosh(L) + \sinh(L)}{(R_{Leak}/R_\infty)\sinh(L) + \cosh(L)}\right) \quad (9)$$

where R_∞ is the input resistance of a semi-infinite cylinder with the same diameter and membrane/axial properties as that of the modeled cylinder; R_{Leak} is the leak resistance at the distal end of the cylinder and L is the cable length in units of λ of the cylinder.

All simulations were performed using NEURON simulator (Carnevale and Hines 2006) running on a grid of 1,800 Intel Xeon 64-bit cores, running Linux 4.

Data analysis, statistics, and reproducibility

Statistical analyses were exclusively 2-sided and made using Graphpad InStat 3 (GraphPad Software, Inc, La Jolla, United States) and Matlab R2009b, 2013 or 2017b

using custom-written software (Mathworks, Natick, United States). The Kolmogorov–Smirnov test was used to determine parametric or nonparametric distribution of an individual dataset and values are presented in text as mean ± standard deviation or median (first quartile–third quartile range) depending on whether data was normally distributed or not, respectively. Nonparametric data are visualized in boxplots (generated in Matlab 2017b) with the central mark as the median, the edges of the box the 25th and 75th percentiles, the whiskers extend to the most extreme data points, and the outliers are plotted individually. Parametric data are presented as bar graphs with mean ± standard deviation. When determining statistical differences between datasets (Fig. 1), we used the unpaired *t*-test when independent datasets followed parametric distributions and the Mann–Whitney test when one or both datasets followed nonparametric distributions. Statistical significance cutoff was $P < 0.05$ and the statistical test used for each analysis is noted with each *P*-value. We used permutation tests for our analyses in Supplemental Fig. S7 since the data do not adhere to the assumptions of equal variances and symmetry. This test computes the mean differences of each possible permutation of observed values for the 2 datasets and returns *P* as the probability of the difference being greater than or equal to that found with the experimental datasets (Wilks 2019).

Excitatory postsynaptic potential (EPSP) peak amplitude was calculated as the average membrane potential from 0.1 ms on either side of the EPSP peak. EPSP rise time was defined as the time (ms) from 10% to 90% of EPSP peak amplitude and response onset was defined as the time at 2% of peak amplitude. Onset latency was the time from presynaptic AP peak to onset of postsynaptic response. Only connections that had >30 recording sweeps were used for failure and coefficient of variation (c.v.) analysis. A response failure event was defined per recording sweep as an event located within 5 ms of the average EPSP peak location with a membrane potential value of <1.5 SD of baseline activity of the postsynaptic neuron. All failure events were detected automatically and verified manually.

Coefficient of variation was calculated as:

$$\text{c.v.} = \frac{\text{standard deviation}}{\text{mean EPSP amplitude}}$$

where both standard deviation and mean EPSP amplitude were calculated only on successful (or "non-fail") events. EPSP potency was calculated as the mean amplitude excluding failed events.

Results

Pyramidal neurons in layers 2 and 3 of human MTG form strong local connections

To investigate pyramidal-to-pyramidal (PN–PN) connectivity in human and mouse, we performed whole-cell patch-clamp recordings of clusters of up to 4 pyramidal neurons in L2/L3 of adult human MTG (Fig. 1a–d and Supplemental Table S1) and L2/3 of adult mouse temporal association area (Fig. 1e–h). We probed for monosynaptic connections by consecutively eliciting a 20-Hz train of 4 action potentials in each neuron of a cluster. All connections depolarized the postsynaptic membrane potential in response to the evoked presynaptic action potential and were therefore considered to be excitatory (Fig. 1c and g, Supplemental Fig. S1). In human, 14% of tested pairs of neurons within a cluster were connected (25 of 185 tested pairs) and this connection probability was similar to that of mouse (12%, 28 of 234 tested pairs, $P = 0.7$, 2-sided Fisher's exact test).

We next analyzed the properties of EPSPs in both species (summarized in Tables 1 and Supplemental Table S4, $n_{human} = 32$ connections, $n_{mouse} = 28$ connections). EPSP onset latency, jitter, and rise time were similar between species (Table 1 and Fig. 1i–k); however the EPSP decay time was significantly longer in human (mean decay human ± standard deviation: 31.3 ± 12.8 ms, mouse: 20.2 ± 9.9 ms, Fig. 1l, $P < 0.01$, unpaired *t*-test). Most notably, median EPSP amplitude was ~3 times larger in human compared with mouse (median EPSP amplitude human, first–third quartile: 1.12 mV (0.54–1.72 mV, $n = 32$ connections), mouse: 0.38 mV (0.23–0.60 mV, $n = 28$ connections), Mann–Whitney test, $P < 0.001$, Fig. 1m and n) and was not correlated to disease severity (Supplemental Fig. S1).

It is important to note that in current-clamp mode, changes in membrane potential resulting from a given input depend on several factors, including the input resistance of the postsynaptic neuron. We found that the input resistance at the soma was significantly lower in human compared with mouse L2/3 neurons (median postsynaptic input resistance human: 64.5 MΩ (50.9–101.2 MΩ), mouse: 94.8 MΩ (60.0–190.1 MΩ), Mann–Whitney test, $P = 0.03$, Supplemental Fig. S3) and therefore does not explain a larger EPSP amplitude in human. This suggests that the synaptic current in human L2/L3–L2/L3 connections is larger. To measure synaptic currents, we next performed recordings in voltage clamp mode (Fig. 1o–q). Excitatory postsynaptic currents (EPSCs) were indeed significantly larger in human compared with mouse, both in peak amplitude (median peak EPSC amplitude human: 17.7 pA (10.3–24.9 pA), mouse: 7.5 pA (5.9–8.1 pA), and Mann–Whitney test, $P < 0.05$) and in total charge (median charge human: 298 fC (228 fC–351 fC), mouse: 102 fC (63 fC–153 fC), Mann–Whitney test, $P < 0.05$).

Pyramidal-to-pyramidal connections in human are more reliable

Next, we wanted to determine how reliable PN–PN connections are in human MTG: How often does a single presynaptic action potential evoke an EPSP in the postsynaptic neuron and, in the case that an EPSP did occur, what was the within-connection variation in its amplitude? We therefore analyzed individual traces of the postsynaptic response to quantify 2 measures of

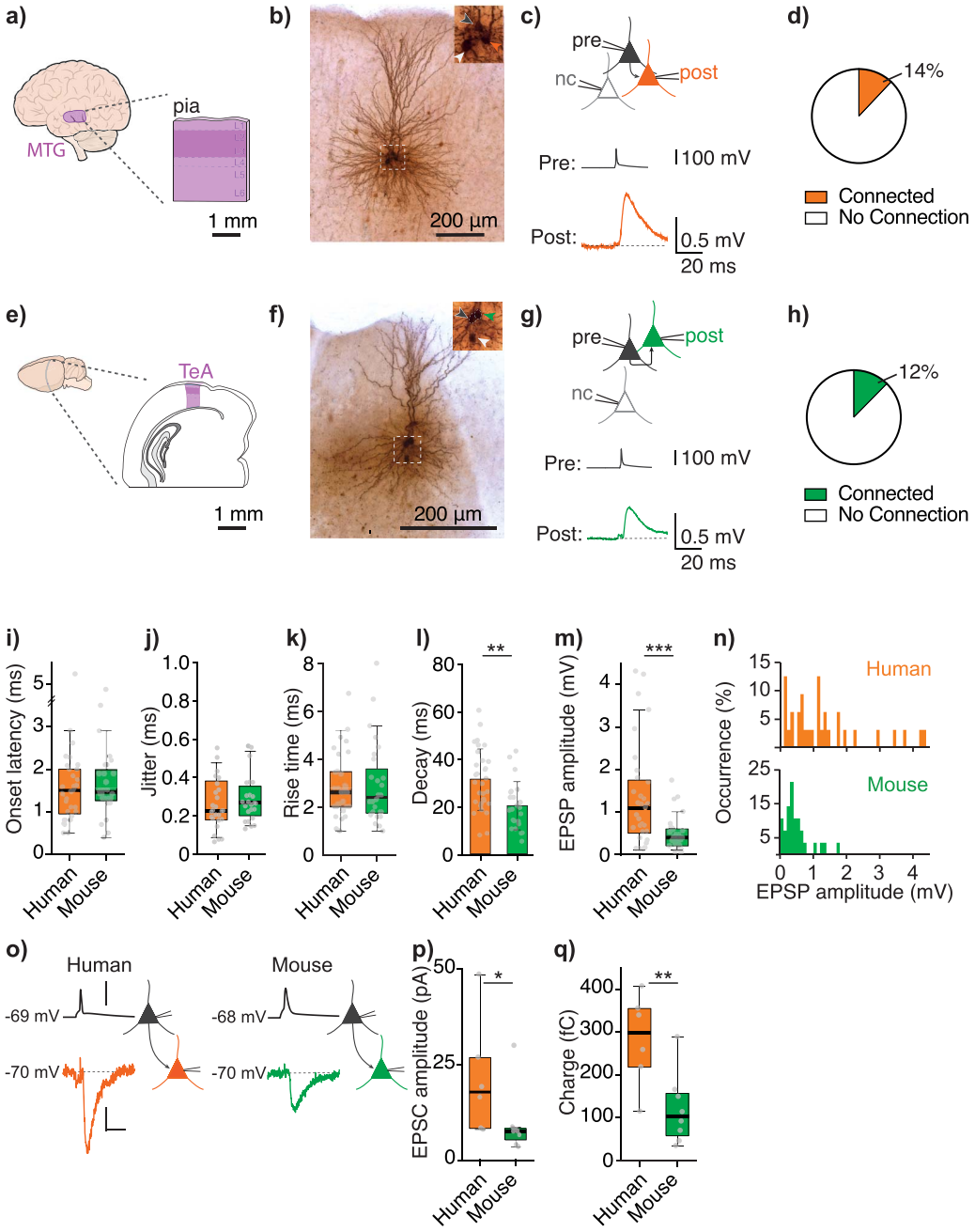

Fig. 1. Local pyramidal-to-pyramidal connections in human MTG are larger in amplitude compared with mouse temporal association area. **a**) Slice configuration of resected human MTG. **b**) Example image of recovered cluster of connected human pyramidal neurons. Inset shows a close up of somas with arrowheads indicating the pre- (black) and postsynaptic (orange) somas, as well as a third soma of an unconnected neuron (white). **c**) Top schematic image depicts the recording configuration of the same cluster of neurons as in **b)** (pre: presynaptic, post: postsynaptic, and nc: no connection). Below example traces are the averaged traces from this cluster showing the evoked action potential in the presynaptic neuron (black trace) and the resulting EPSP in the connected postsynaptic neuron (orange). **d**) Pie graph showing connection rate in human for 157 tested pairs of neurons (14%, 25 of 185 tested pairs were connected). Only connections where we also stored the corresponding number of "no connection" tested pairs during the experimental session were counted for this analysis. **e–h)** Show the same as above but in mouse temporal association area (TeA). Postsynaptic neurons are represented in green (**f–h)** and mouse connection rate shown in **h**) was 12% ($n = 28$ of 234 tested pairs of neurons, $P = 0.7$, Fisher's exact test). **i**) Average onset latency ($P = 0.6$, Mann–Whitney test). **j**) Average onset latency jitter ($P = 0.3$, Mann–Whitney test), dotted line indicates cut-off jitter for monosynaptic EPSPs (Lalanne et al. 2016). **k)** Median rise time ($P = 0.7$, Mann–Whitney test). **l**) Mean decay time constant ($P < 0.01$, unpaired t-test). **m**) n median amplitude ($P < 0.001$, Mann–Whitney test) of EPSPs in human (orange) and mouse (green). **o**) Schematic images and example traces of human and mouse connections in voltage clamp with presynaptic neurons and their traces depicted in black and postsynaptic neurons and their traces in orange (human) or green (mouse). Membrane potential values at the left of each trace correspond to the resting membrane potential for presynaptic traces and the holding potential for postsynaptic traces. Scalebars 100 mV, 5pA, and 10 ms. **p**) Median amplitude of excitatory postsynaptic currents (EPSC, $P = 0.03$, Mann–Whitney test). **q**) Median response charge ($P = 0.008$, Mann–Whitney test). Boxplots in Fig. 1 (and Figs. 2–4 and Supplemental Figures) show median as central mark, the edges of the box the 25th and 75th percentiles, the whiskers extend to the most extreme data points, and the outliers are plotted individually.

Table 1. Summary of EPSPs properties.

Species	Amplitude (mV) median	Amplitude (mV) mean	Onset latency (ms) median	Rise time (ms) median	Decay (ms) mean	Failure rate (%) median	C.v. mean	Potency (mV) median
Human	1.12 (0.54–1.72) ($n = 32$)	1.36 ± 1.19 ($n = 32$)	1.5 (1.0–2.0) ($n = 32$)	2.6 (2.0–3.5) ($n = 32$)	31.3 ± 12.8 ($n = 31$)	0 (0–4) ($n = 29$)	0.2 ± 0.1 ($n = 28$)	1.10 (0.53–1.94) ($n = 29$)*
Mouse	0.38 (0.23–0.60) ($n = 28$)	0.49 ± 0.41 ($n = 28$)	1.4 (1.3–2.0) ($n = 28$)	2.4 (1.8–3.4) ($n = 28$)	20.2 ± 9.9 ($n = 23$)	25 (10–34) ($n = 24$)	0.4 ± 0.1 ($n = 22$)	0.48 (0.28–0.57) ($n = 24$)**
P-value	0.0007 (MW)	–	0.60 (MW)	0.68 (MW)	< 0.01 (*t*-test)	< 0.0001 (MW)	<0.0001 (*t*-test)	0.0014 (MW)

Note: Median (first quartile—third quartile) and mean ± standard deviation of each EPSP property for human and mouse. Number of connections used for measurement of each property is indicated. * Corresponding $n = 29$ human connections (1.10 mV, 0.53–1.70). ** Corresponding $n = 24$ mouse connections (0.34 mV, 0.21–0.53).

reliability: failure rate and coefficient of variation (c.v., Fig. 2). For both human and mouse, we considered a successful response to be membrane depolarization that is larger than 1.5 standard deviation (SD) of the baseline noise activity of the postsynaptic neuron, a standard cutoff in the literature (Feldmeyer et al. 2006). Human PN–PN connections rarely failed, with a median failure rate of 0% (0–4%, $n = 29$ connections) and were therefore much more reliable compared with mouse connections, which had a median failure rate of 25% (10–34%), $n = 24$ connections, Mann–Whitney test, $P < 0.0001$, Fig. 2a–d. This significant difference was also present in voltage clamp experiments (Fig. 1o–q, failure rate 0%, 0–0%, and $n = 6$ human connections, 7%, 4–11%, and $n = 8$ mouse connections, Mann–Whitney test, $P < 0.05$).

We next performed further analyses to ensure that the species difference in synaptic failure rates was not simply an artifact of how we defined a failed response event. First, the SD of baseline fluctuations was similar in both species (mean human SD: 0.09 mV, range 0.03–0.2, mouse SD: 0.1, range 0.04–0.2, unpaired *t*-test, $P = 0.8$); membrane deflections therefore had to attain a similar membrane potential difference from baseline to be counted as a successful response event. In addition, we quantified failure rates for all connections based on 4 different failure cutoffs: from 1.5 to 4 times SD of baseline activity (Supplemental Fig. S4). Increasing the failure cutoff from 1.5 through to 4 times SD of baseline activity will lead to false failure assignments but as this almost exclusively impacted mouse connections, increasing the failure cutoff only increased the difference in failure rates between human and mouse (median failure rate with 4SD cut-off human: 3% (0–8%), mouse: 55% (40–74%), Mann–Whitney test, $P < 0.0001$).

Given the higher failure rate in mouse compared with human, where an individual presynaptic action potential almost always resulted in a postsynaptic response, it was important to determine whether the difference in EPSP amplitude between species was simply due to a higher number of failed episodes lowering the average EPSP amplitude in mouse. We therefore also calculated EPSP potency (i.e. average peak of successful response episodes only) and found that it was still significantly larger in human (median potency human: 1.10 mV (0.53–1.94 mV, $n = 29$), mouse: 0.48 mV (0.28–0.57 mV, $n = 24$), Mann–Whitney test, $P < 0.01$, Fig. 2e–f).

Furthermore, when a postsynaptic response did occur, the amplitude of a single EPSP varied less in human compared with mouse: human EPSP amplitude was more stable sweep-to-sweep (mean coefficient of variation: 0.2 ± 0.1, mouse: 0.4 ± 0.1, unpaired *t*-test, $P < 0.0001$, Fig. 2g). Finally, in a subset of connections where we recorded postsynaptic responses to a train of presynaptic action potentials (Fig. 2h), we were able to extract utilization of synaptic efficacy *U* through fitting the EPSPs to the Tsodyks–Markram model (TM-model, see Methods). In the TM-model, "*U*" represents the percentage of resources used at the presynaptic level when an action potential occurs (Markram et al. 1998; Fuhrmann et al. 2002; Ecker et al. 2020). Consistent with a more reliable synapse, human utilization of synaptic efficacy was significantly higher than mouse (median *U* human: 0.55 (0.39–0.70), mouse: 0.33 (0.23–0.42), Mann–Whitney test, $P < 0.05$, Fig. 2i).

The TM-model was additionally used to extract *D* ($\tau_{recovery}$ from depression) and *F* ($\tau_{recovery}$ from facilitation): *D* human: 309.3 ms (140.6–678.6), mouse: 468.5 ms (145.9–2239.7), *F* human: 1.7 ms (0.4–421.9), and mouse: 4.7 ms, (0.1–152.7). Thus, human synapses recover faster from depression compared with mouse synapses (Testa-Silva et al. 2014).

Synaptic communication between morphologically identified pyramidal neurons

We next turned to the anatomical analysis of connected neurons to determine wiring properties of local connections. We have previously shown that pyramidal neurons in L2/L3 of human MTG belong to at least 2 distinct morphological cell types: profuse- and slim-tufted pyramids (Deitcher et al. 2017), characterized by elaborate and simple branching properties of the apical dendrite, respectively. Based on findings in rodent neocortex (Brown and Hestrin 2009), cellular morphology may correspond to specific wiring motifs and functional roles. We therefore asked which cell types were involved in local connections. Slim- and profuse-tufted neurons follow

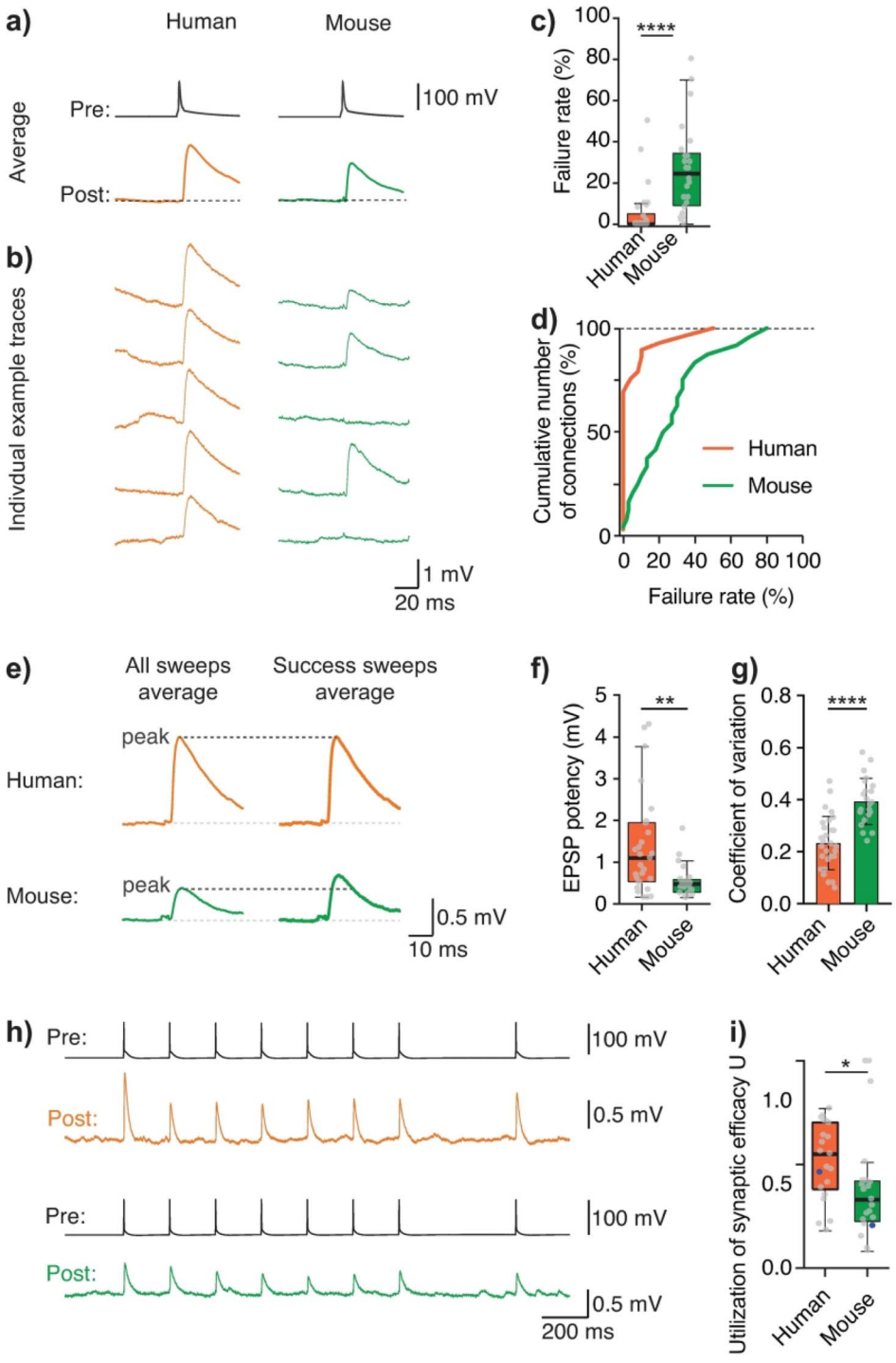

Fig. 2. Human local pyramidal-to-pyramidal connections are reliable. **a**) Example connections show average presynaptic AP and postsynaptic EPSP traces for human (orange) and mouse (green). **b**) Traces correspond to example individual traces from those same connections. **c**) Median failure rates ($P < 0.0001$, Mann–Whitney test). **d**) Cumulative distribution of failure rates for human and mouse. **e**) Example average traces for all traces, including failed events (left) and only counting success sweeps (right) show that EPSP amplitude of "success-only" traces (i.e. EPSP potency) was still larger in human. **f**) Median EPSP potency ($P < 0.01$, Mann–Whitney test). **g**) Mean c.v. was significantly larger in mouse connections ($P < 0.0001$, unpaired *t*-test). **h**) Example traces for human (top, presynaptic trace in black, postsynaptic trace in orange) and mouse (bottom, presynaptic trace in black, postsynaptic trace in green) of postsynaptic responses to a 5 Hz train and recovery pulse of presynaptic action potentials. **i**) Median utilization of synaptic efficacy, *U* ($P < 0.05$, Mann–Whitney test), blue datapoints correspond to the example connections shown in **h**).

distinct localization gradients within L2/L3: profuse-tufted neurons are mostly located within the first 200–800 μm from pia (but full range of possible locations spans 200–1200 μm from pia), whereas the majority of slim-tufted neurons were identified between 800 and 1200 μm from pia ($n = 87$ identified single neurons, cumulative data across projects, Fig. 3a). Because our neurons were located throughout L2/L3 (Fig. 3b and Supplemental Fig. S5), we could not rely on spatial location alone to determine which types of neurons were included in our

recordings. Therefore, we morphologically reconstructed the apical dendrites of a subset of connected neurons. This subset consisted of neurons where the apical dendrites of both the pre- and postsynaptic neurons were preserved in the slice without major truncations (Fig. 3c). Using these reconstructions, we classified the neurons into profuse- and slim-tufted types as in our previous study (Deitcher et al. 2017). Briefly, the procedure involves constructing a topological profile from the apical dendrite branching structure (Kanari et al. 2018). This profile is transformed into a persistence diagram in which branch and termination points reflect the underlying structure of the morphology. The persistence diagrams are used to train a classifier, which estimates the likelihood of newly added morphologies to represent either profuse- or slim-tufted pyramids. Morphologies with a moderate tuft do not classify clearly (cutoff < 90% prediction accuracy) and are classified as "ambiguous." Of the $n = 11$ reconstructed neurons, 7 were identified as profuse-tufted, 1 was ambiguous and 3 were slim-tufted pyramids (Fig. 3d). This allowed us to identify 4 profuse-to-profuse connections (one reciprocal), 1 ambiguous-to-profuse, and 2 slim-to-slim-tufted connections (1 presynaptic pyramid targeting 2 different postsynaptic neurons). The $n = 1$ ambiguous-to-profuse connection (EPSP amplitude 0.4 mV) and $n = 2$ slim-to-slim connections (EPSP amplitude 2.0 and 3.8 mV) were both from a single patient and not statistically compared with the total population. Electrophysiological properties of the subset of $n = 4$ profuse-to-profuse connections (from $N = 3$ patients) were comparable with the total population (Fig. 3e–f, median EPSP amplitude: 1.32 mV (0.83–1.72 mV), median failure rate: 0% (0–4%), Mann–Whitney, $P > 0.05$).

Synaptic wiring principles between L2/L3 pyramidal cells are maintained across species

PN–PN connections in human MTG are stronger (Fig. 1) and more reliable (Fig. 2) compared with mouse. This may be due to a combination of factors including a higher number of synapses per connection or larger synaptic conductance. To determine which structural and synaptic parameters might best explain species differences in connection strength, we analyzed the number and location of putative synapses between pre- and postsynaptic neurons in 5 human PN–PN connections and 4 mouse connections. We digitally reconstructed the pre- and postsynaptic neurons (including presynaptic axon) and determined for each pair the number and location of putative synapses (i.e. cross-over between presynaptic axon and postsynaptic dendrite in the same focal plane (Markram et al. 1997; Feldmeyer et al. 2002; Yang et al. 2021; Fig. 3g, Supplemental Table S5), a subset of putative synapses is illustrated across focal planes in Supplemental Fig. S6). To determine the number of putative synaptic contacts, close appositions of presynaptic axon terminals and postsynaptic dendrites were searched for under light-microscopy and the presynaptic axon from the parent pyramidal soma reconstructed to the target dendrites of the postsynaptic pyramid (Molnar et al. 2016).

Number of putative synapses per connection was similar between species: human connections had on average 4.0 ± 1.2 putative synapses and mouse connections had on average 3.2 ± 1.3 putative synapses (Fig. 3h). It must be noted that we identified a small number of synapses per connection that we could not reliably trace back to the presynaptic neuron. The total number of detected putative synapses was however still similar between species after including these "orphan" putative synapses (human: 5.4 ± 1.1 detected putative synapses, mouse: 5.0 ± 0.8 detected putative synapses, Supplemental Table S5). These numbers are comparable with the number of putative contacts for other connections between pairs of excitatory cortical neurons in rodents (Frick et al. 2008; Yang et al. 2021), including cases in which putative contacts found with light-microscopy were confirmed using high-resolution electron microscopy (Markram et al. 1997; Feldmeyer et al. 2002; Yang et al. 2021). Finally, numbers represent "putative" synapses and should ideally be confirmed with super resolution light-microscopy or (correlated) electron microscopy (Holler et al. 2021). In addition, we cannot exclude the possibility that the number of synapses for connected pairs in human and/or mouse is underestimated due to truncation of (apical) dendritic or axonal trees (Supplemental Figs. S8 and S9; van Pelt et al. 2014).

Human putative L2/L3–L2/L3 synapses were located on both basal and apical dendrites, and those located on apical dendrites were mainly on obliques (Fig. 3i). Despite the overall large size of pyramidal neurons in human L2/L3 (Mohan et al. 2015) and the fact that we often observed axon in the vicinity of apical tufts, putative synapses were located relatively proximally to the soma (human mean dendritic distance to soma: 146.7 ± 54.4 μm, Fig. 3i), at a similar dendritic distance to soma compared with mouse (141.2 ± 25.4 μm, $P = 0.8$, unpaired t-test, Welch's correction).

Pyramidal-to-pyramidal connections in human are associated with large AMPA and NMDA conductances

To uncover the properties of synaptic connections, we constructed detailed compartmental models that reconciled electrophysiological experiments and morphologies of the postsynaptic cells. Compartmental models of 4 postsynaptic human neurons were constructed; 5 human EPSPs were fitted as 1 human neuron was postsynaptic to 2 different presynaptic neurons (Fig. 4, Supplemental Fig. S8, see Methods). Compartmental models of 4 postsynaptic mouse neurons were also constructed. For both human and mouse, these models incorporated dendritic spines (see Supplemental Table S2 for human and mouse spine parameters). To quantify the effect of apical dendrite truncation on biophysical properties, we

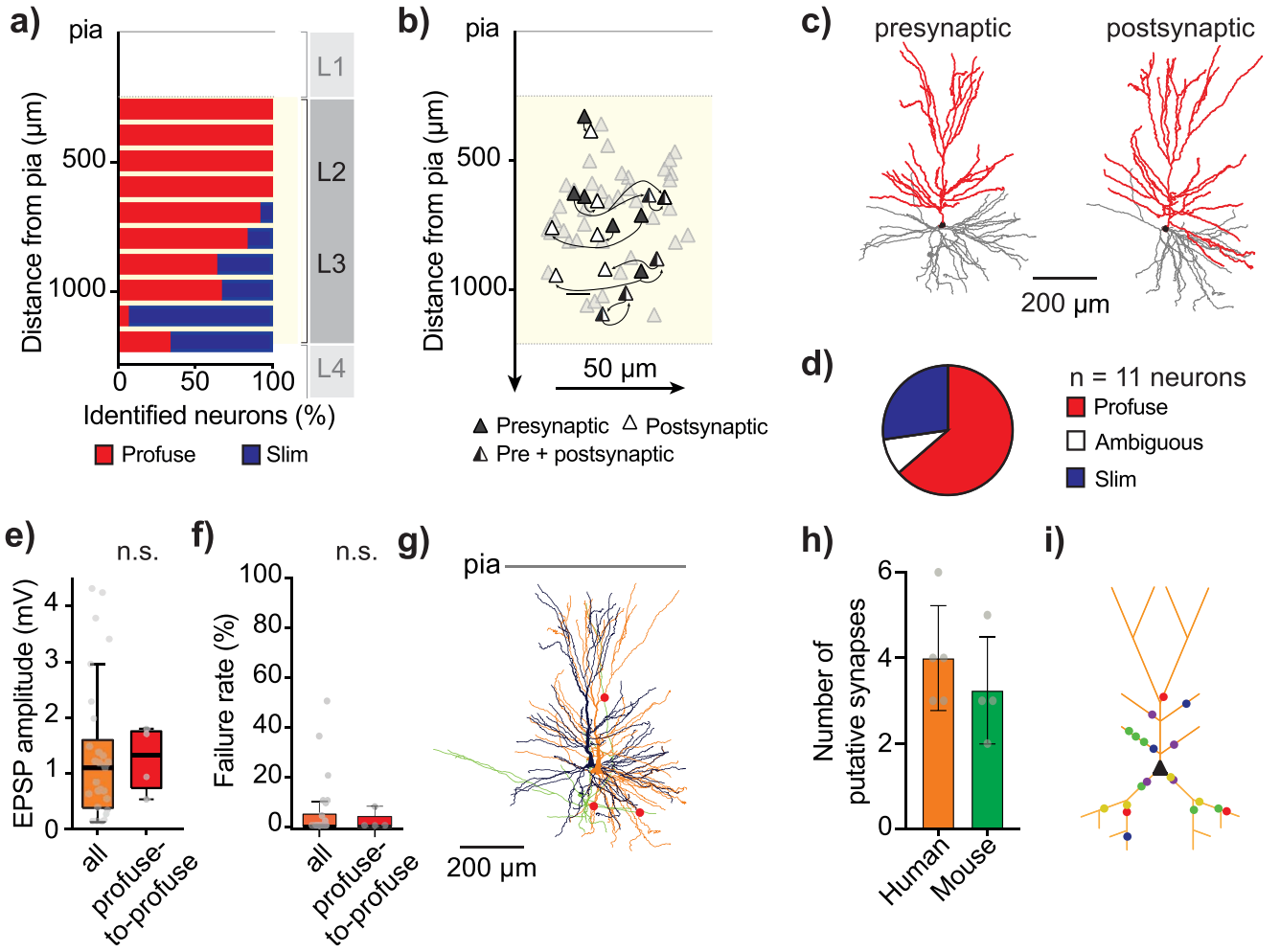

Fig. 3. Morphological and anatomical analysis of local connections in L2/L3 of human MTG. **a**) Distribution of identified single neurons throughout L2/L3 of human MTG [total of 87 identified single neurons of which 60 were already identified for a previous study (Deitcher et al. 2017) and 27 were newly identified here], with profuse-tufted neurons ($n = 58$ neurons) in red and slim-tufted neurons ($n = 29$ neurons) in blue. **b**) Distribution within L2/L3 of recorded clusters where soma-pia distances were recorded through microdrive coordinates. *X*-axis distance between neurons of the same cluster is true to scale but *X*-axis distance between clusters is not and has been randomly chosen for clarity. **c**) Example morphological reconstruction (soma and apical dendrites in red, basal dendrites in gray) of 2 connected neurons (left: presynaptic, right: postsynaptic neuron). **d**) Pie graph showing number of identified neurons per cell-type (8 profuse-tufted neurons and 2 "ambiguous" type neurons, forming 4 profuse-to-profuse and 2 ambiguous-to-profuse type connections). **e**) Median EPSP amplitude of identified profuse-to-profuse connections relative to the full population of this study (excluding the identified profuse-profuse connections). **f**) Median fail rate of identified profuse-to-profuse connections relative to the full population of this study (excluding the identified profuse-profuse connections). **g**) Reconstructed connected pair of neurons from Fig. 1 (presynaptic neuron in black with axon in green, postsynaptic neuron in orange and putative synapse locations in red). Images of putative synapses for this connection in Fig. S6. **h**) Human presynaptic neurons formed on average 4.0 ± 1.2 putative synapses ($n = 5$ connections) onto their postsynaptic neuron comparable with mouse average number of putative synapses: 3.2 ± 1.1, ($n = 4$ connections). **i**) Schematic postsynaptic neuron depicting locations of all putative synapses from 5 distinct connections in L2/L3 human MTG. Putative synapses were located in basal dendrites and proximal apical dendrites (total mean distance from soma: 147 ± 54 μm) and were at similar dendritic distances to mouse (mouse total mean dendritic distance to soma: 141 ± 26 μm).

performed feature extraction on an independent dataset of complete and truncated morphologies and found comparable values for rheobase, input resistance, and spike threshold, amplitude and width (all $P > 0.05$, Supplemental Table S6) and concluded that truncation of the apical dendrite did not significantly affect biophysical parameters as measured from the soma.

First, for each postsynaptic neuron, we fitted the subthreshold experimental response to 1-s-long hyperpolarizing current pulses. Under the assumption of specific axial resistance of $R_a = 250$ Ω cm (Eyal et al. 2018) the models predicted that the mean value for the specific membrane resistivity, R_m, in human L2/L3 pyramidal cells is 32 ± 5 kΩ cm^2; see example in Fig. 4a and b). Next, we extracted the membrane time constant and the first equalizing time constants (τ_0 and τ_1, respectively) from the experimental transient response to a brief current pulse, using Rall's "peeling" method (Rall 1969a, 1969b). This provided an estimate for the electrotonic (cable) length L_{peel} for each neuron (Fig. 4c). L2/L3 human pyramidal neurons are, electrotonically, relatively compact with an average cable length ranging between 0.5–1.4 λ for human and 0.5–1.8 λ for mouse (Supplemental Fig. S8 and see also Eyal et al. (2018)). The membrane time constant, τ_0, of these neurons ranges between 21–31 ms for human and 16–46 ms for mouse, and the specific

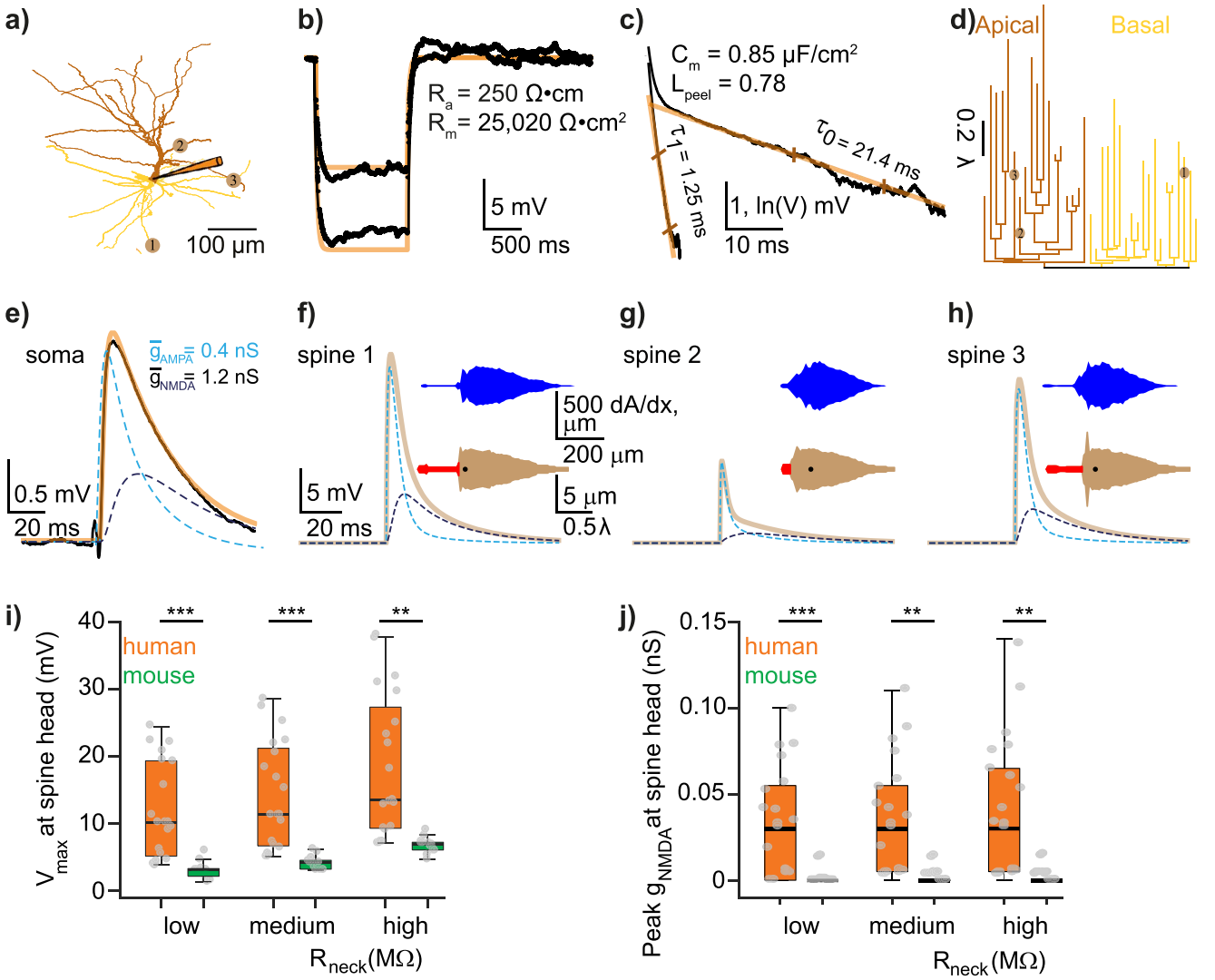

Fig. 4. Properties of human L2/3–L2/3 synapses extracted via matching detailed neuron model to experimental pair-recordings. **a**) Modeled human L2/L3 neuron with dendritic locations of 3 synaptic contacts (numbered circles) originating from a single presynaptic L2/L3 neuron. Apical and basal trees are marked in dark and light orange respectively, schematic electrode at soma is also shown. **b**) Somatic voltage response (black traces) for the neuron shown in **a)** to 2 steady hyperpolarizing current inputs (here, −62 and −108 pA) and the corresponding model fit (brown traces) with respective model values for R_a and R_m. **c**) "Peeling" of somatic voltage transient in response to a brief (2 ms) hyperpolarizing step current (not shown) in the neuron shown in **a**). τ_0, extracted from this peeling, together with R_m as in **b**), are used to calculate C_m, whereas L_{peel} value is computed from τ_1 and τ_0 (see Methods). **d**) Electrotonic dendrograms of the neuron shown in **a**, with locations of the three synaptic contacts. **e**) Experimental somatic EPSP (black trace) in response to a presynaptic spike with model fit superimposed (light brown). Synapses were activated on modeled dendritic spines (see Supplemental Fig. S9 and Methods). AMPA- and NMDA- components of the modeled EPSP are also shown (dashed lines) with their respective maximal conductances value (at each synaptic contact). The NMDA-component is calculated by subtracting the AMPA component of the EPSP from the AMPA- plus NMDA-based EPSP. **f–g)** Computed EPSPs and respective AMPA- and NMDA-components at the spine head membrane located at the three synaptic sites shown in **a)**. The upper (blue) and lower (red/brown) insets show, respectively, the spatial distribution of the neuron's membrane area **a**) as a function of the physical distance, x, from the spine and the "equivalent cable" as seen from the spine perspective (spine is located at left end of these insets, soma location is marked by the black dot, see Methods). Observing the "equivalent cable" insets, the electrotonic decoupling of spine #1 and #3 from the impedance load due to the respective red cable (at the left of inset) results in relatively large EPSPs at these spines, whereas the large impedance load that is adjacent to spine #2 results in a relatively small EPSP at this spine. **i**) Computed EPSP peak at the spine head membrane for human (orange) and mouse (green) connections for different spine-neck resistances (R_{neck}). Low: $R_{neck\ human}$: 68.8 MΩ, $R_{neck\ mouse}$: 37.2 MΩ (these values were computed with spine dimensions as in Supplemental Table S2 and R_a = 250 Ω cm), medium: 200 MΩ for both human and mouse and high: 500 MΩ, for human and mouse respectively. Note that EPSP peak at the spine head membrane remains significantly larger in human also for a R_{neck} of 200 MΩ and 500 MΩ. **j**) as in **i**), now showing the NMDA peak conductance for each individual spine head for different R_{neck} cases. Low: $R_{neck\ human}$: 68.8 MΩ, $R_{neck\ mouse}$: 37.2 MΩ. Medium: 200 MΩ and high: 500 MΩ, respectively.

membrane capacitance (C_m) ranges between 0.73 and 0.85 $\mu F/cm^2$ (mean 0.79 ± 0.02 $\mu F/cm^2$, compared with mouse mean C_m: 1.1 ± 0.5 $\mu F/cm^2$, see Eyal et al. (2016)).

Having the dendritic location of the putative synapses, which originated from a single presynaptic neuron, the model enabled us to estimate both the properties of the local EPSP at the spine head receiving the synaptic input and the respective AMPA- and NMDA-based conductances that give rise to the experimental somatic EPSP (Fig. 4e and Supplemental Fig. S8). Notably, the local EPSP amplitude varied substantially between the different spines contacted by a single presynaptic axon

(Fig. 4f–h). Given that in our model the properties of individual spiny synapses are identical for all synaptic contacts, this large difference in EPSP amplitude between spines must be due to the difference in impedance load (the "sink") imposed by the dendritic tree on the respective spine. To better understand how the "dendritic environment" of the spine impacts the synaptic potential at the spine, we developed a new approach by computing the "equivalent cable" of the whole dendritic tree as viewed from the spine perspective (Fig. 4f–h, lower red/brown cables at insets and Supplemental Fig. S8, see Methods). As illustrated in Fig. 4f–h, when the large impedance load (the expanded brown part of the respective cable in insets) is electrically adjacent to the spine (shorter red cable at insets), there is a significant current loss from the spine to the dendritic sink and, consequently, the resultant EPSP at the spine head membrane is relatively small (Fig. 4g). In contrast, EPSPs are relatively large in spines that are more electrically decoupled from the dendritic sink (longer red cable at insets of Fig. 4f and h).

Due to the extended dendritic morphology of human pyramidal neurons and increased length of terminal dendrites (Deitcher et al. 2017), human synapses were typically more electrically decoupled from the adjacent dendritic sink compared with mouse synapses. This, on its own (assuming all other parameters were the same), predicts that the local EPSPs are expected to be larger in human spines (Fig. 4i and Supplemental Fig. S8). Our model also predicts that the AMPA component in human synapses is significantly larger compared with mouse (mean AMPA-conductance in human: 0.47 ± 0.1 nS, mouse 0.16 ± 0.02 nS, $P = 0.03$, permutation test, Supplemental Fig. S8). Consequently, the EPSP amplitude at the input spine is almost 4 times larger in human compared with mouse (median EPSP amplitude at spine in human is 11.9 ± 7.1 mV and in mouse, 3.0 ± 1.2 mV, $P < 0.0001$, unpaired t-test, Welch's correction, Fig. 4i, 2 left bars and Supplemental Fig. S8). Such relatively large depolarization in human spines recruits a significant NMDA conductance component (median spine NMDA conductance in human: 0.032 nS (0.005–0.053 nS) and in mouse, 0.000 nS (0.000–0.001 nS), $P = 0.0008$ Mann–Whitney test, Fig. 4j, orange vs green bars at left).

We further analytically simplified the "equivalent cables," as viewed by individual spiny synapses, to respective "equivalent cylinders" with leaky ends, demonstrating that these cylinders faithfully predict the time-integrals (the charge) generated by the excitatory synapse impinging on the spine head, even in the case of nonlinear NMDA-dependent synaptic currents (Supplemental Fig. S8). This computation further explained the boosted EPSP's peak and increased NMDA-conductance at the spine head in human versus mouse. Interestingly, our computations also show that, in both human and mouse, the somatic EPSP arising from multiple synaptic contacts made by a single presynaptic L2/L3 axon is, in most cases, a linear sum of the effect of its individual synaptic contacts (median (first–third Quartile range) of EPSP amplitude for individual synaptic contacts at soma; human: $n = 20$, 0.54 mV (0.33–0.65), mouse: $n = 13$, 0.14 mV (0.09–0.20)).

Dendritic spines come in a variety of shapes and dimensions, which affect a key electrical parameter, the spine-neck resistance (R_{neck}). R_{neck} is proportional to the length of the spine neck and reciprocally proportional to the square of the spine-neck diameter (see Equation (1) above). The larger R_{neck} is, the more electrically decoupled is the spine head (the synapse) from the spine base, and the larger is the input impedance at the spine head membrane (Rall 1974; Segev and Rall 1988). Recent studies indicate a large variability in spine-neck diameter, ranging between 0.05 and 0.3 μm, which implies (Equation (1)) that R_{neck} may range between 30 and 500 MΩ with neck length of ~1 μm and specific axial resistance ~150–250 Ω cm (Harnett et al. 2012; Tonnesen et al. 2014). In Fig. 4i and j, we utilized our model to examine the effect of R_{neck} on the EPSP amplitude and the NMDA peak conductance in human versus mouse spines. Towards this end, for each R_{neck} value (and corresponding to different spine-neck diameters, Supplemental Table S2), we computed the synaptic parameters at the respective spines that give rise to the experimental somatic EPSP (as in Fig. 4e). The orange and green bars in the middle and right side of Fig. 4i demonstrate that the EPSP peak at the spine head membrane remains significantly larger in human even for medium R_{neck} value of 200 MΩ (human: 14.1 ± 7.0 mV, mouse: 4.1 ± 1.0 mV, $P < 0.0001$, unpaired t-test, Welch's correction) and large R_{neck} of 500 MΩ (human: 18.3 ± 10.6 mV, mouse: 6.8 ± 1.2 mV, $P = 0.0001$, unpaired t-test, Welch's correction). Similarly, Fig. 4j shows that the NMDA peak conductance remains significantly larger in human versus mouse synapses for both medium R_{neck} of 200 MΩ (human: 0.032 nS (0.005–0.055 nS), mouse: 0.004 nS (0.000–0.004 nS), $P < 0.0001$, Mann–Whitney test) and large R_{neck} of 500 MΩ (human: 0.033 nS (0.006–0.067 nS), mouse: 0.004 nS (0.000–0.004 nS), $P < 0.0001$, Mann–Whitney test). We conclude that the expected EPSP peak at the spine head membrane and, consequently, the recruited NMDA conductance are significantly larger in human versus mouse for a variety of spine morphologies/R_{neck} values (see Discussion).

Finally, we validated whether our findings on large voltage changes and significant NMDA peak conductance in human spines depend on 2 model assumptions: (i) the number of putative synapses, and (ii) uniformity of synaptic AMPA-conductance in all synaptic contacts formed by a given presynaptic axon. Towards this end, we first reduced the number of putative synapses per modeled connection by a factor of 0.4 (see Holler et al. 2021), after which the number of putative synapses in the model were rounded up to the next integer (see Supplemental Table S5 for individual values). For our $n = 5$ human pairs and $n = 4$ mouse pairs, this resulted in a random removal of 45% and 44% of putative synapses, respectively. We found that even with such a significant

reduction in the number of putative synapses, simulations still show that human spines experience significantly larger EPSP amplitude and increased NMDA peak conductance compared with mouse (Supplemental Fig. S10, Mann–Whitney, $P < 0.001$ for both parameters).

Second, we enabled in the model variable AMPA-conductance across the original number of putative synapses within a connection (as opposed to uniform AMPA-conductance across spines, Fig. 4). The model then searches for the parameter space of different combinations of AMPA-conductances across individual spines that optimally reproduce the experimental somatic EPSP. Under these conditions, we again found that both EPSP amplitude and NMDA peak conductance are significantly larger in human spines compared with mouse (Supplemental Fig. S10, Mann–Whitney, $P < 0.01$ for EPSP amplitude and $P < 0.0001$ for NMDA peak conductance, respectively).

We experimentally validated the model predictions on postsynaptic NMDA receptor function during synaptic transmission by testing the effect of the selective NMDA-receptor antagonist AP5 (50 μM) on EPSP amplitude and decay kinetics (example experiment in Fig. 5a). These somatic recordings do not allow quantification of NMDA contribution at the level of individual spines, but indicate the NMDA contribution for the sum of synaptic contacts at the level of the soma (including dendritic filtering and attenuation). Since the modeling revealed that NMDA receptor conductance varied between unitary connections, we first tested the sensitivity to AP5 by comparing sweep amplitude of individual connections for baseline versus AP5 conditions (Fig. 5b). In human, 4 out of 7 connections showed a significant reduction in EPSP amplitude upon AP5 application (Fig. 5c, 4 out of 7, $P < 0.05$, Mann–Whitney), thus confirming the model predictions. In 3 out of 7 connections, we found a reduction in EPSP amplitude, but this reduction did not reach statistical significance ($P > 0.05$, Mann–Whitney). For mouse, we found a reduction in EPSP amplitude upon AP5 application in 3 out of 4 connections, but the reduction reached statistical significance in only 1 out of 4 connections and the effect of the AP5 on EPSP decay was variable (Fig. 5c).

For connections in human MTG, we found that AP5 application resulted in a decrease in EPSP amplitude in all $n = 7$ connections in human MTG (on average 23% reduction, Fig. 5e, $P < 0.05$, Wilcoxon, signed-rank test). We also found that AP5 application resulted in a decrease of EPSP decay time constant in all connections (hence faster EPSP kinetics), reaching statistical significance at the population level (on average 17% reduction, Fig. 5e, $P < 0.05$, $n = 7$, Wilcoxon, signed-rank test), further substantiating the contribution of NMDA receptor activation to synaptic transmission in human MTG. In mouse L2/3 TeA unitary connections, we did not find consistent effect of AP5 on both EPSP amplitude or decay kinetics (Fig. 5d, $P > 0.05$, Mann–Whitney).

In a subset of human unitary connections, we tested the effect of blocking both NMDA and AMPA receptors (50 μm AP5 + 10 μm NBQX), which in all cases completely abolished the postsynaptic response ($n = 4$, median amplitude aCSF: 0.49 mV, 0.18–1.18 mV, AP5 + NBQX: 0.01 mV, 0.006–0.017 mV, $P = 0.03$, Friedman test). This indicates that for connected pairs of human L2/L3 pyramidal neurons, postsynaptic responses involve activation of both AMPA and NMDA receptors. We thus provide experimental validation that synaptic transmission across unitary (excitatory) connections involves prominent activation of NMDA receptors in human MTG L2/L3.

Discussion

Although characteristics such as cortical layering and cell architecture are conserved across species, human cortical neurons have a number of divergent anatomical and functional properties relative to mouse (Mohan et al. 2015; Eyal et al. 2018; Bakken et al. 2021; Berg et al. 2021; Kalmbach et al. 2021). Through multiple whole-cell recordings of clusters of up to 4 neurons, we show that morphologically identified pyramidal neurons in L2/L3 of human MTG (Brodmann area 21) form strong and reliable local connections with low trial-to-trial variability. Connection frequency and EPSP onset kinetics are similar to those of mouse in the same recording conditions, whereas connection amplitude is approximately 3-fold larger at the soma and failure rate significantly lower in human (0% vs 25% failure rate for human and mouse, respectively). Strong and reliable human synapses are consistent with the modeled higher synaptic conductance and higher release probability in human, respectively. We identified the morphological subclass (profuse- vs slim-tufted pyramids, Deitcher et al. 2017) in a validation dataset of connected human neurons in our data and found putative synaptic contacts occurring in proximal basal and oblique dendrites between pairs of profuse-tufted pyramids, supporting previous modeled estimations of synapse location for local human connections (Eyal et al. 2018). Modeling additionally reveals that due to the combination of larger synaptic conductance, dendritic cable structure, and synapse location in L2/L3 human neurons, EPSP amplitude is significantly larger at human spines. This is primarily due to the fact that human dendrites are structurally more extended (Mohan et al. 2015; Deitcher et al. 2017) and thus electrically more distributed (i.e. larger average cable length). Consequently, dendritic synapses are, on average, more electrically isolated from the rest of the dendritic tree as compared with mouse synapses. This implies larger local input resistance in human at the synaptic (spine) locations. Consequently, the spine head resistance is, on average, larger in human vs that of the mouse and thus the EPSP amplitude (and NMDA recruitment) is expected to be larger in human spines just based on morphological characteristics, for a wide range of spine-neck diameters (R_{neck} values). As a consequence, spine depolarization is sufficient to activate NMDA current at the spine

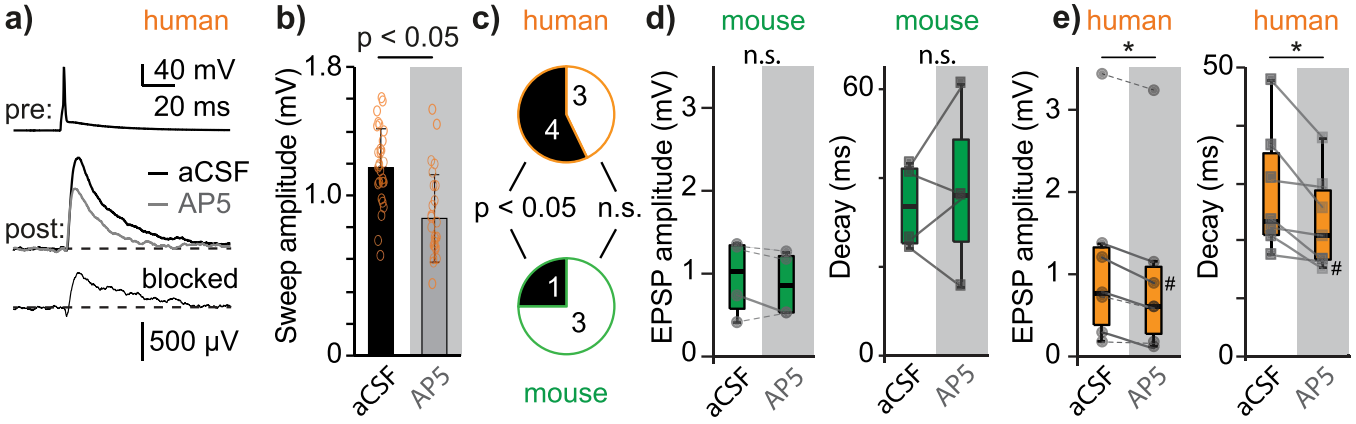

Fig. 5. NMDA receptor activation contributes to unitary EPSPs in human but not in mouse connections. **a**) Example average traces for a pyramidal-to-pyramidal connection in L2/L3 human MTG. Pre: presynaptic neuron; post: postsynaptic neuron. Control EPSP in black (aCSF), EPSP after application of NMDA receptor blocker AP5 (50 μM) in gray. The depolarization blocked by AP5 is labeled "blocked" and generated by subtracting the AP5 EPSP from the aCSF EPSP. **b)** Single sweep amplitude during aCSF (black) and AP5 (gray) conditions for the example connection from I1 ($P < 0.05$, Mann–Whitney test). **c**) In human, 4 out of 7 connections showed a significant reduction of EPSP amplitude upon AP5 application and in mouse, 1 out of 4 connections, respectively. **d**) Effect of AP5 on EPSP amplitude (left) and decay (right) in mouse. **e**) Effect of AP5 on EPSP amplitude (left, $n = 7$, $P < 0.05$, Wilcoxon, signed-rank test) and EPSP decay (right, $n = 7$, $P < 0.05$, Wilcoxon, signed-rank test) for human unitary connections. # Denotes example from Fig. 5a and b. Note that AP5 has inconsistent effect on mouse EPSP amplitude and decay ($n = 4$) but consistently reduces EPSP amplitude and decay kinetics for individual human unitary connections ($n = 7$).

head membrane in a unitary connection; this prediction was directly validated experimentally (Fig. 5). The L2/L3 pyramidal-to-pyramidal microcircuit of human MTG is thus characterized by strong and reliable synaptic transmission that includes activation of NMDA receptors in the absence of action potential spiking in the postsynaptic neuron.

Experimental and theoretical studies have shown that strong recurrent excitation combined with the activation of the slow NMDA receptors are necessary for generating persistent neuronal activity (Wang 1999; Wang et al. 2013). Modeling work also showed that slow, NMDA-dependent reverberation provides a circuit mechanism for the maintenance of working memory representations, as well as for semantic processing and decision-making computations (Adler et al. 1998; Wang et al. 2013; Wang 2020). These features of human synaptic transmission (the high reliability and NMDA-component in recurrent L2/L3–L2/L3 excitatory connections) may thus contribute to language-related processing streams in humans and might underlie associations within the distributed semantic network.

Tissue limitations

All human tissue used for this study arose from patients who required surgery for either epilepsy focal point removal or tumor removal. To avoid potential influence of disease state on our results, we restricted tissue samples to cortical tissue that was distal from the focal site of epilepsy or location of tumor (which was typically located subcortically). We also restricted our recordings to a well-defined location in MTG (Fig. 1a, Brodmann area 21, 2–6 cm from the temporal pole). Furthermore, we have previously found that a number of human single cell properties do not depend on disease type, state, or duration (Testa-Silva et al. 2010; Verhoog et al. 2013; Testa-Silva et al. 2014; Mohan et al. 2015; Goriounova et al. 2018). In the current study, EPSP strength and reliability also did not correlate with severity or duration of disease (Supplemental Fig. S2). Taken together with the fact that recent histological and electrophysiological analysis has shown that the very large majority of distally resected tissue is itself nonpathological in terms of levels of markers and electrophysiological properties (Berg et al. 2021; Pegasiou et al. 2020), the data available suggests that our results on synaptic strength are generalizable for the human population.

Functionally strong and reliable synapses in human MTG

We provide the first functional evidence that local morphologically identified PN–PN connections in MTG are larger and more reliable in human compared with mouse, in anatomically comparable regions. Compared with other adult rodent PN–PN connections observed in the literature (somatosensory, visual, and auditory cortices; Reyes and Sakmann 1999; Oswald and Reyes 2008; Seeman et al. 2018), mouse EPSP amplitude in the present study is comparable. The higher EPSP amplitude in human is likely in part due to a higher upper bound in amplitude distribution (maximum $EPSP_{human}$ amplitude: 4.3 mV, maximum $EPSP_{mouse}$ amplitude: 1.7 mV). The stronger connections in human are not due to a larger number of synaptic contacts (Fig. 3). Rather, it is explained by the larger presynaptic active zones and postsynaptic densities in human that may allow higher release probability (Fig. 2) as well as more neurotransmitter release and binding (Benavides-Piccione et al. 2002; Yakoubi et al. 2019), ultimately leading to larger synaptic conductance at human synapses (Fig. 4 and Supplemental Fig. S7). Such anatomical properties, together with a high release probability and

a strong and reliable postsynaptic response suggest that multivesicular release may occur at human PN–PN synapses, as has already been suggested for human pyramidal-to-interneuron cortical synapses (Molnar et al. 2016). Our cable modeling study also shows that geometrical considerations per se, which lead to the electrically more isolated dendritic spines in human dendrites, significantly enhance the recruitment of NMDA current in human synapses and, consequently, to a larger EPSP at the spine head and at the soma.

Interestingly, connection frequency does not differ in our mouse and human samples, despite human pyramidal neurons theoretically having higher availability to form connections, with more complex dendritic branching (Mohan et al. 2015) and higher spine densities and total spine count (Benavides-Piccione et al. 2002; Eyal et al. 2018). Indeed, we find that the number of putative synapses per local connection is similar between species (4.0 vs 3.2 for human vs mouse, respectively); human pyramidal neurons may instead receive and incorporate more inputs from longer-range projections rather than local ones (Schmidt et al. 2021).

A recent study that investigated local pyramidal connectivity in human temporal cortex reported a similar connection frequency in human L2/L3 (~15%) but a considerably smaller median EPSP amplitude (L2: 0.22 mV, L3: 0.34 mV; Seeman et al. 2018). Given the very similar connection rate, this difference in amplitude is likely due to different experimental conditions, making direct comparison difficult. In particular, the combination of a lower aCSF calcium concentration (1.3 mM compared with our 2 mM), which leads to lower release probability, and an algorithm-based detection threshold (with a minimum amplitude of ~10 μV compared with our ~50 μV), likely impacted median EPSP amplitude. Our experimental design on the other hand (2-mM calcium), allows direct comparison with published values of synaptic strength for a wide range of excitatory connections across cortical regions. This comparison shows that EPSP amplitude for pyramidal-to-pyramidal connections in supragranular layers is highest in human MTG (relative to L2/3 in rodent temporal, primary visual, and somatosensory cortices; Holmgren et al. 2003; Feldmeyer et al. 2006; Lefort et al. 2009; Jiang et al. 2015; Luo et al. 2017). Relative to human L2/L3 MTG, EPSP amplitude can be higher for excitatory connections in rodent primary somatosensory cortex layers 4 and 5 (Markram et al. 1997; Feldmeyer et al. 1999; Feldmeyer et al. 2002; Frick et al. 2008; Qi et al. 2017). Variability in EPSP amplitude (or synaptic efficacy) across studies may be in part explained by analysis method (average vs median value) or detection power (Campagnola et al. 2022; Supplemental Fig. S14), but we can also not exclude the possibility that variability causally links to species differences (rat vs mouse vs human), age (juvenile, adolescent, and adult; Frick et al. 2007; Campagnola et al. 2022) or region (primary visual cortex vs primary somatosensory cortex vs association cortex; Holmgren et al. 2003; Feldmeyer et al. 2006).

Furthermore, here we have used 4 electrodes (instead of 8, (Seeman et al. 2018; Campagnola et al. 2022) or even 10 (Peng et al. 2019)) and entirely manual patching to probe for local connections. Our strategy may have allowed for better preservation of neuronal processes as it was suggested recently that increased number of simultaneous recorded neurons may lead to (for instance) mechanical instability or electrical noise (Qi et al. 2020). In general, our results are supported by proof-of-concept evidence from other laboratories that used comparable experimental conditions (e.g. 2-mM calcium in the recording aCSF) and also describe connections within a similar amplitude range as ours (Molnar et al. 2008; Peng et al. 2019). In addition, (Campagnola et al. 2022) conclude that human L2/L3 EPSPs are larger in human temporal cortex compared with mouse primary visual cortex. Finally, anatomical studies conducted on pyramidal synapses in human temporal cortex collectively show enlarged active zones, vesicle pools, spine size, and postsynaptic density (Benavides-Piccione et al. 2002; Molnar et al. 2016; Yakoubi et al. 2019). These studies thus provide evidence that human excitatory synapses have the structural properties to support strong and reliable synaptic transmission.

Functional implications

Pyramidal neurons in a local network composed of relatively strong intrinsic connections with low amplitude variability will be capable of initiating action potentials with relative ease, requiring input from fewer neighboring neurons. Yet sparse action potential firing is an important feature of information coding in L2/3 of rodent sensory cortices (Barth and Poulet 2012) and is likely maintained by local inhibition. If sparse firing is a conserved feature in human cortical circuits then local inhibition must also be increased to counterbalance the increased ease to generate action potentials in human temporal cortex. Indeed, GABAergic neurons in human motor cortex are twice as common in proportion compared to mouse (Hornung and De Tribolet 1994; Bakken et al. 2021). Furthermore, human pyramidal neurons can evoke large glutamatergic EPSPs in neighboring GABAergic interneurons, which can generate firing in these interneurons with only milliseconds delay and as such may aid in maintaining the E–I balance (Szegedi et al. 2016; Szegedi et al. 2017). The strength and function of human inhibitory synapses and their organization in L2/L3 temporal cortex will be essential to uncover in future studies (Boldog et al. 2018; Obermayer et al. 2018; Poorthuis et al. 2018).

Here, we identify a subset of these locally connected pyramidal neurons as profuse-tufted type neurons (Deitcher et al. 2017). Further investigation into the molecular identity of connected neurons and their downstream targets will shed light on the function of these local connections in information processing (Brown and Hestrin 2009). Indeed, at least 24 distinct excitatory molecular types of neurons have been described in human temporal cortex, with at least 5

distinct excitatory cell types present in L2 or L3 and divergent expression of glutamate receptors (Hodge et al. 2019). Furthermore, a number of these pyramidal transcriptomic cell types display distinct morphological and electrophysiological characteristics (Berg et al. 2021); probing connections of known morphological or molecular types will allow precise building of circuit simulations and predictions of their functional roles. Furthermore, study of the modulation of local connections would also shed light on the benefits and disadvantages of such an adaptation, such as serotonin which is known to be divergently expressed in human cortex (Hodge et al. 2019). It is equally important to uncover cell-type specific function and wiring motifs in human cortex in view of brain disease. For instance, L2/L3 cortico-cortical projections may play a role in neuroanatomical changes leading to autism (Velmeshev et al. 2019) and increased L2/L3 excitatory neurotransmission has been implicated in onset of multiple sclerosis (Beutel et al. 2020). Thus, questions on cell-type specific properties of connections in L2/L3 or directionality within the wiring motif may be the focus of future work.

Finally, the distinct anatomical and membrane properties (e.g. large and complex dendrites, lower membrane capacitance, and higher h-channel density) of human pyramidal neurons directly impact signal propagation (Eyal et al. 2014; Mohan et al. 2015; Eyal et al. 2016; Kalmbach et al. 2018; Gidon et al. 2020). Using a novel method to study the impact of the dendritic tree on the spiny-synapse, we found that the extended spread of human dendrites allows for human synapses to be relatively electrically decoupled from the impedance sink imposed on the spine by the rest of the dendritic tree. The resulting electrical isolation, in conjunction with a higher synaptic conductance, allows for a significantly larger spine EPSP that recruits NMDA receptors at the spine head (Figs. 4 and 5 and Supplemental Fig. S7). Thus, in a subset of adult human unitary excitatory connections in vitro, a single presynaptic spike is sufficient to activate postsynaptic NMDA receptors and trigger calcium influx, in the absence of postsynaptic action potential spiking (Beaulieu-Laroche and Harnett 2018). Similar conditions were previously observed in juvenile mouse connections with large EPSP amplitude (1.0 mV, somatosensory cortex, S1; Feldmeyer et al. 2006; Sarid et al. 2015). This increased EPSP amplitude for juvenile S1 at the soma relative to our adult mouse TeA data (EPSP amplitude: 0.38 mV) could be due to reduced electrical isolation of dendritic branches or larger EPSP amplitude at the spine. Independent of the underlying local properties of dendrites and spines, is thus tempting to conclude that a strong unitary EPSP is sufficient to trigger local NMDA receptor activation, since we did not observe NMDA receptor activation upon unitary synaptic transmission in adult mouse TeA connections.

Whether NMDA receptor activation is attained more commonly in human purely because of the larger spine EPSP or in addition to distinct receptor subunit or synapse protein composition remains to be determined (Emes and Grant 2012; Paoletti et al. 2013) but is highly relevant for further study since receptor configuration directly impacts functions such as voltage dependency, Mg^{2+} sensitivity and Ca^{2+} permeability (Paoletti et al. 2013). An increased ability to activate these receptors could alter multiple fundamental properties of the microcircuit, including NMDA receptor-dependent plasticity, the rules of which are already known to be inversed in some cases in human (Verhoog et al. 2013). Since synaptic plasticity is key to basic functions of the central nervous system, including learning and memory formation (Citri and Malenka 2008), it will be crucially important to identify the neurophysiological constraints underlying human synapse plasticity, as they may deviate from murine principles on important aspects (Verhoog et al. 2013; Testa-Silva et al. 2014; Lenz et al. 2021).

A direct NMDA receptor activation could also implicate less reliance on backpropagating action potentials for NMDA receptor activation in some synapses and thus lowering the threshold for local dendritic nonlinearities by facilitating NMDA spikes (Schiller et al. 2000). Finally, what could be the impact of strong and reliable local connections in vivo? Interestingly, the strength of local recurrent excitation is thought to determine the ability of a local circuit to sustain reverberating activity, a phenomenon that underlies working memory (Wang 2001; Driesen et al. 2013; Wang et al. 2013; Wang 2020). The stronger the recurrent excitation is within a local circuit in vivo, the more likely these circuits will uphold persistent network activity, and this also largely depends on the activation of NMDA receptors (Adler et al. 1998; Wang 1999). In turn, blocking NMDA receptor function with NMDA-receptor antagonist ketamine has a negative impact on verbal performance and working memory (Adler et al. 1998). Our findings therefore suggest that—through efficient recruitment of NMDA receptors—human temporal cortex may in fact be better equipped to accommodate persistent activity and thus also an enhanced working memory, which in turn may be key to semantic and language processing (Hickok and Poeppel 2007; Binder et al. 2009).

To conclude, we provide functional evidence for strong, reliable, and consistent synapses in human MTG, in direct alignment of robust anatomical evidence that indicate human-specific synaptic properties relative to rodent. As such, our mechanistic insights provide a first step towards larger-scale simulations of human cortical circuits as has already been achieved for rodent (Markram et al. 2015) or macaque (Joglekar et al. 2018). Furthermore, a number of neurological and psychiatric disorders have been associated to subtle disruptions in neurotransmission, function of individual cell-types or microcircuit wiring in human brain. This includes cortico-cortical neurons in autism spectrum disorder (Shepherd 2013; Velmeshev et al. 2019), deep layer

excitatory neurons in Major Depressive Disorder (Nagy et al. 2020), layer 5 pyramidal tract neurons in ALS (Shepherd 2013), or NMDA receptor function as critical factor across a multitude of neurological and psychiatric disorders (Paoletti et al. 2013; Beutel et al. 2020). Our results highlight the vital importance of further studying the fundamental properties of human local circuits to not only bridge the gap in cross-scale understanding the human brain in health but also broaden the perspective on successful human-specific treatments in disease patients (Garey et al. 1998; Cummings et al. 2014; Wong et al. 2019).

Acknowledgments

We thank Profs. Guus Smit, Maarten Kole, and Srikanth Ramaswamy for critical discussions on a previous version of this manuscript and Anton Pieneman and Anna Galakhova for assistance during histology.

Supplementary material

Supplementary material is available at *Cerebral Cortex* online.

Funding

This study was supported by funding to the Blue Brain Project, a research center of the Ecole Polytechnique fédérale de Lausanne (EPFL), by support from the Swiss government's ETH Board of the Swiss Federal Institutes of Technology, by The Spanish "Ministerio de Ciencia e Innovación" (grant PGC2018-094307-B-I00) and by the Center for Neurogenomics and Cognitive Research (Vrije Universiteit Amsterdam Amsterdam). HDM received funding for this work from the US Brain Initiative by the National Institutes of Health under Award Number U01MH114812, the European Union's Horizon 2020 Framework Programme for Research and Innovation under the Specific Grant Agreement No. 945539 (Human Brain Project SGA3), and Nederlandse Organisatie voor Wetenschappelijk Onderzoek (NWO) Gravitation program BRAINSCAPES: A Roadmap from Neurogenetics to Neurobiology (NWO: 024.004.012). IS received generous support from the Drahi family foundation, from the European Union's Horizon Framework Program for Research and Innovation under the Specific Grant Agreement No. 785907 (Human Brain Project SGA2), the ETH domain for the Blue Brain Project, the Gatsby Charitable Foundation, and the NIH Grant Agreement U01MH114812.

Conflict of interest statement. None declared.

Authors' contributions

CdK, IS, HDM, HM, FS, ESL, SH, and YL designed the study, SH, RW, NAG, MBV, GTS, JO, DBH, TH, and MMK prepared slices and performed EPhys recordings, SH managed data, SH, LK, IS, and CdK analyzed data, RBP and JDF analyzed spine morphology, YL and IS performed the compartmental modeling; NBZ performed modeling to extract release probability; SH, EM, RA, and CdK performed Neurolucida reconstructions; SH and NAG performed histology; TV analyzed histology; PdW, SI, DN, and JCB performed surgeries on human patients; SH, CdK, YL, and IS wrote the manuscript with input from all authors.

Data availability

The datasets generated during and/or analyzed during the current study are available from the corresponding author on reasonable request.

Data was collected within the framework of this project and we did not specifically attempt to replicate the current dataset.

Code availability

The codes used during the current study are available from the corresponding author on reasonable request.

References

Adler CM, Goldberg TE, Malhotra AK, Pickar D, Breier A. Effects of ketamine on thought disorder, working memory, and semantic memory in healthy volunteers. *Biol Psychiatry*. 1998:43:811–816.

Assaf Y, Bouznach A, Zomet O, Marom A, Yovel Y. Conservation of brain connectivity and wiring across the mammalian class. *Nat Neurosci*. 2020:23:805–808.

Bakken TE, Jorstad NL, Hu Q, Lake BB, Tian W, Kalmbach BE, Lein ES. Comparative cellular analysis of motor cortex in human, marmoset and mouse. *Nature*. 2021:598:111–119.

Barros-Zulaica N, Rahmon J, Chindemi G, Perin R, Markram H, Muller E, Ramaswamy S. Estimating the readily-releasable vesicle Pool size at synaptic connections in the neocortex. *Front Synaptic Neurosci*. 2019:11.

Barth AL, Poulet JF. Experimental evidence for sparse firing in the neocortex. *Trends Neurosci*. 2012:35:345–355.

Beaulieu-Laroche L, Harnett MT. Dendritic spines prevent synaptic voltage clamp. *Neuron*. 2018:97:75–82 e73.

Beaulieu-Laroche L, Toloza EHS, van der Goes MS, Lafourcade M, Barnagian D, Williams ZM, Harnett MT. Enhanced dendritic compartmentalization in human cortical neurons. *Cell*. 2018:175:643–651.e614.

Benavides-Piccione R, Ballesteros-Yanez I, DeFelipe J, Yuste R. Cortical area and species differences in dendritic spine morphology. *J Neurocytol*. 2002:31:337–346.

Benavides-Piccione R, Fernaud-Espinosa I, Robles V, Yuste R, DeFelipe J. Age-based comparison of human dendritic spine structure using complete three-dimensional reconstructions. *Cereb Cortex*. 2013:23:1798–1810.

Benavides-Piccione R, Regalado-Reyes M, Fernaud-Espinosa I, Kastanauskaite A, Tapia-Gonzalez S, Leon-Espinosa G, DeFelipe J. Differential structure of hippocampal CA1 pyramidal neurons in the human and mouse. *Cereb Cortex*. 2020:30:730–752.

Berg J, Sorensen SA, Ting JT, Miller JA, Chartrand T, Buchin A, Lein ES. Human neocortical expansion involves glutamatergic neuron diversification. *Nature*. 2021:598:151–158.

Beutel T, Dzimiera J, Kapell H, Engelhardt M, Gass A, Schirmer L. Cortical projection neurons as a therapeutic target in multiple sclerosis. *Expert Opin Ther Targets*. 2020:24:1211–1224.

Binder JR, Desai RH, Graves WW, Conant LL. Where is the semantic system? A critical review and meta-analysis of 120 functional neuroimaging studies. *Cereb Cortex*. 2009:19:2767–2796.

Boldog E, Bakken TE, Hodge RD, Novotny M, Aevermann BD, Baka J, Tamas G. Transcriptomic and morphophysiological evidence for a specialized human cortical GABAergic cell type. *Nat Neurosci*. 2018:21:1185–1195.

Brown SP, Hestrin S. Intracortical circuits of pyramidal neurons reflect their long-range axonal targets. *Nature*. 2009:457: 1133–1136.

Buckner RL, Krienen FM. The evolution of distributed association networks in the human brain. *Trends Cogn Sci*. 2013:17:648–665.

Burke RE, Fleshman JW, Segev I. Factors that control the efficacy of group Ia synapses in alpha-motoneurons. *J Physiol Paris*. 1988:83: 133–140.

Campagnola L, Seeman SC, Chartrand T, Kim L, Hoggarth A, Gamlin C, Jarsky T. Local connectivity and synaptic dynamics in mouse and human neocortex. *Science*. 2022:375:eabj5861.

Carnevale NT, Hines ML. *The Neuron Book*. Cambridge (UK): Cambridge University Press; 2006.

Citri A, Malenka RC. Synaptic plasticity: multiple forms, functions, and mechanisms. *Neuropsychopharmacology*. 2008:33:18–41.

Cummings JL, Morstorf T, Zhong K. Alzheimer's disease drug-development pipeline: few candidates, frequent failures. *Alzheimers Res Ther*. 2014:6:37.

Deitcher Y, Eyal G, Kanari L, Verhoog MB, Atenekeng Kahou GA, Mansvelder HD, Segev I. Comprehensive morpho-electrotonic analysis shows 2 distinct classes of L2 and L3 pyramidal neurons in human temporal cortex. *Cereb Cortex*. 2017:27:5398–5414.

Douw L, Nissen IA, Fitzsimmons S, Santos FAN, Hillebrand A, van Straaten ECW, Goriounova NA. Cellular substrates of functional network integration and memory in temporal lobe epilepsy. *Cereb Cortex*. 2021:32(11):2424–2436.

Driesen NR, McCarthy G, Bhagwagar Z, Bloch MH, Calhoun VD, D'Souza DC, Krystal JH. The impact of NMDA receptor blockade on human working memory-related prefrontal function and connectivity. *Neuropsychopharmacology*. 2013:38:2613–2622.

Ecker A, Romani A, Saray S, Kali S, Migliore M, Falck J, Ramaswamy S. Data-driven integration of hippocampal CA1 synaptic physiology in silico. *Hippocampus*. 2020:30:1129–1145.

Egger V, Nevian T, Bruno RM. Subcolumnar dendritic and axonal organization of spiny stellate and star pyramid neurons within a barrel in rat somatosensory cortex. *Cereb Cortex*. 2008:18:876–889.

Elston GN, Benavides-Piccione R, DeFelipe J. The pyramidal cell in cognition: a comparative study in human and monkey. *J Neurosci*. 2001:21:RC163.

Emes RD, Grant SGN. Evolution of synapse complexity and diversity. *Annu Rev Neurosci*. 2012:35:111–131.

Eyal G, Mansvelder HD, de Kock CPJ, Segev I. Dendrites impact the encoding capabilities of the axon. *J Neurosci*. 2014:34:8063–8071.

Eyal G, Verhoog MB, Testa-Silva G, Deitcher Y, Lodder JC, Benavides-Piccione R, Segev I. Unique membrane properties and enhanced signal processing in human neocortical neurons. *Elife*. 2016:5.

Eyal G, Verhoog MB, Testa-Silva G, Deitcher Y, Benavides-Piccione R, DeFelipe J, Segev I. Human cortical pyramidal neurons: from spines to spikes via models. *Front Cell Neurosci*. 2018:12:181.

Feldmeyer D, Egger V, Lubke J, Sakmann B. Reliable synaptic connections between pairs of excitatory layer 4 neurones within a single 'barrel' of developing rat somatosensory cortex. *J Physiol*. 1999:521(Pt 1):169–190.

Feldmeyer D, Lubke J, Silver RA, Sakmann B. Synaptic connections between layer 4 spiny neurone-layer 2/3 pyramidal cell pairs in juvenile rat barrel cortex: physiology and anatomy of interlaminar signalling within a cortical column. *J Physiol*. 2002:538: 803–822.

Feldmeyer D, Lubke J, Sakmann B. Efficacy and connectivity of intracolumnar pairs of layer 2/3 pyramidal cells in the barrel cortex of juvenile rats. *J Physiol*. 2006:575:583–602.

Frick A, Feldmeyer D, Sakmann B. Postnatal development of synaptic transmission in local networks of L5A pyramidal neurons in rat somatosensory cortex. *J Physiol*. 2007:585:103–116.

Frick A, Feldmeyer D, Helmstaedter M, Sakmann B. Monosynaptic connections between pairs of L5A pyramidal neurons in columns of juvenile rat somatosensory cortex. *Cereb Cortex*. 2008:18(2): 397–406.

Fuhrmann G, Segev I, Markram H, Tsodyks M. Coding of temporal information by activity-dependent synapses. *J Neurophysiol*. 2002:87:140–148.

Garey LJ, Ong WY, Patel TS, Kanani M, Davis A, Mortimer AM, Hirsch SR. Reduced dendritic spine density on cerebral cortical pyramidal neurons in schizophrenia. *J Neurol Neurosurg Psychiatry*. 1998:65:446–453.

Gidon A, Zolnik TA, Fidzinski P, Bolduan F, Papoutsi A, Poirazi P, Larkum ME. Dendritic action potentials and computation in human layer 2/3 cortical neurons. *Science*. 2020:367:83–87.

Goldberg DE, Holland JH. Genetic algorithms and machine learning. *Mach Learn*. 1988:3:95–99.

Goriounova NA, Heyer DB, Wilbers R, Verhoog MB, Giugliano M, Verbist C, Mansvelder HD. Large and fast human pyramidal neurons associate with intelligence. *elife*. 2018:7.

Harnett MT, Makara JK, Spruston N, Kath WL, Magee JC. Synaptic amplification by dendritic spines enhances input cooperativity. *Nature*. 2012:491:599–602.

Heyer DB, Wilbers R, Galakhova AA, Hartsema E, Braak S, Hunt S, Goriounova NA. Verbal and general IQ associate with supragranular layer thickness and cell properties of the left temporal cortex. *Cereb Cortex*. 2022:32(11):2343–2357.

Hickok G, Poeppel D. The cortical organization of speech processing. *Nat Rev Neurosci*. 2007:8:393–402.

Hodge RD, Bakken TE, Miller JA, Smith KA, Barkan ER, Graybuck LT, Lein ES. Conserved cell types with divergent features in human versus mouse cortex. *Nature*. 2019:573:61–68.

Holler S, Kostinger G, Martin KAC, Schuhknecht GFP, Stratford KJ. Structure and function of a neocortical synapse. *Nature*. 2021:591(7848):111–116.

Holmgren C, Harkany T, Svennenfors B, Zilberter Y. Pyramidal cell communication within local networks in layer 2/3 of rat neocortex. *J Physiol*. 2003:551:139–153.

Horikawa K, Armstrong WE. A versatile means of intracellular labeling: injection of biocytin and its detection with avidin conjugates. *J Neurosci Methods*. 1988:25:1–11.

Hornung JP, De Tribolet N. Distribution of GABA-containing neurons in human frontal cortex: a quantitative immunocytochemical study. *Anat Embryol (Berl)*. 1994:189:139–145.

Jacobs B, Schall M, Prather M, Kapler E, Driscoll L, Baca S, Treml M. Regional dendritic and spine variation in human cerebral cortex: a quantitative golgi study. *Cereb Cortex*. 2001:11:558–571.

Jahr CE, Stevens CF. Voltage dependence of NMDA-activated macroscopic conductances predicted by single-channel kinetics. *J Neurosci*. 1990:10:3178–3182.

Jiang X, Shen S, Cadwell CR, Berens P, Sinz F, Ecker AS, Tolias AS. Principles of connectivity among morphologically defined cell types in adult neocortex. *Science*. 2015:350:aac9462.

Joglekar MR, Mejias JF, Yang GR, Wang XJ. Inter-areal balanced amplification enhances signal propagation in a large-scale circuit model of the primate cortex. *Neuron*. 2018:98:222–234 e228.

Kalmbach BE, Buchin A, Long B, Close J, Nandi A, Miller JA, Ting JT. H-channels contribute to divergent intrinsic membrane properties of supragranular pyramidal neurons in human versus mouse cerebral cortex. *Neuron*. 2018:100:1194–1208.e1195.

Kalmbach BE, Hodge RD, Jorstad NL, Owen S, de Frates R, Yanny AM, Ting JT. Signature morpho-electric, transcriptomic, and dendritic properties of human layer 5 neocortical pyramidal neurons. *Neuron*. 2021:109:2914–2927 e2915.

Kanari L, Dlotko P, Scolamiero M, Levi R, Shillcock J, Hess K, Markram H. A topological representation of branching neuronal morphologies. *Neuroinformatics*. 2018:16:3–13.

Lalanne T, Abrahamsson T, Sjostrom PJ. Using multiple whole-cell recordings to study spike-timing-dependent plasticity in acute neocortical slices. *Cold Spring Harb Protoc*. 2016:2016.

Lefort S, Tomm C, Floyd Sarria JC, Petersen CC. The excitatory neuronal network of the C2 barrel column in mouse primary somatosensory cortex. *Neuron*. 2009:61:301–316.

Lenz M, Kruse P, Eichler A, Straehle J, Beck J, Deller T, Vlachos A. All-trans retinoic acid induces synaptic plasticity in human cortical neurons. *elife*. 2021:10.

Luo H, Hasegawa K, Liu M, Song WJ. Comparison of the upper marginal neurons of cortical layer 2 with layer 2/3 pyramidal neurons in mouse temporal cortex. *Front Neuroanat*. 2017:11:115.

Maass W, Natschläger T, Markram H. Real-time computing without stable states: a new framework for neural computation based on perturbations. *Neural Comput*. 2002:14:2531–2560.

Markram H, Lubke J, Frotscher M, Roth A, Sakmann B. Physiology and anatomy of synaptic connections between thick tufted pyramidal neurones in the developing rat neocortex. *J Physiol*. 1997:500(Pt 2): 409–440.

Markram H, Wang Y, Tsodyks M. Differential signaling via the same axon of neocortical pyramidal neurons. *Proc Natl Acad Sci U S A*. 1998:95:5323–5328.

Markram H, Muller E, Ramaswamy S, Reimann MW, Abdellah M, Sanchez CA, Schurmann F. Reconstruction and simulation of neocortical microcircuitry. *Cell*. 2015:163:456–492.

McDaniel MA. Big-brained people are smarter: a meta-analysis of the relationship between in vivo brain volume and intelligence. *Intelligence*. 2005:33:337–346.

Mohan H, Verhoog MB, Doreswamy KK, Eyal G, Aardse R, Lodder BN, de Kock CP. Dendritic and axonal architecture of individual pyramidal neurons across layers of adult human neocortex. *Cereb Cortex*. 2015:25:4839–4853.

Molnar G, Olah S, Komlosi G, Fule M, Szabadics J, Varga C, Tamas G. Complex events initiated by individual spikes in the human cerebral cortex. *PLoS Biol*. 2008:6:e222.

Molnar G, Rozsa M, Baka J, Holderith N, Barzo P, Nusser Z, Tamas G. Human pyramidal to interneuron synapses are mediated by multi-vesicular release and multiple docked vesicles. *Elife*. 2016:5.

Nagy C, Maitra M, Tanti A, Suderman M, Theroux JF, Davoli MA, Turecki G. Single-nucleus transcriptomics of the prefrontal cortex in major depressive disorder implicates oligodendrocyte precursor cells and excitatory neurons. *Nat Neurosci*. 2020:23:771–781.

Obermayer J, Heistek TS, Kerkhofs A, Goriounova NA, Kroon T, Baayen JC, Mansvelder HD. Lateral inhibition by Martinotti interneurons is facilitated by cholinergic inputs in human and mouse neocortex. *Nat Commun*. 2018:9:4101.

Oswald AM, Reyes AD. Maturation of intrinsic and synaptic properties of layer 2/3 pyramidal neurons in mouse auditory cortex. *J Neurophysiol*. 2008:99:2998–3008.

Paoletti P, Bellone C, Zhou Q. NMDA receptor subunit diversity: impact on receptor properties, synaptic plasticity and disease. *Nat Rev Neurosci*. 2013:14:383–400.

Pegasiou CM, Zolnourian A, Gomez-Nicola D, Deinhardt K, Nicoll JAR, Ahmed AI, Vargas-Caballero M. Age-dependent changes in synaptic NMDA receptor composition in adult human cortical neurons. *Cereb Cortex*. 2020:30:4246–4256.

Peng Y, Mittermaier FX, Planert H, Schneider UC, Alle H, Geiger JRP. High-throughput microcircuit analysis of individual human brains through next-generation multineuron patch-clamp. *Elife*. 2019:8:e48178.

Poorthuis RB, Muhammad K, Wang M, Verhoog MB, Junek S, Wrana A, Letzkus JJ. Rapid neuromodulation of layer 1 interneurons in human neocortex. *Cell Rep*. 2018:23:951–958.

Qi G, van Aerde K, Abel T, Feldmeyer D. Adenosine differentially modulates synaptic transmission of excitatory and inhibitory microcircuits in layer 4 of rat barrel cortex. *Cereb Cortex*. 2017:27: 4411–4422.

Qi G, Yang D, Ding C, Feldmeyer D. Unveiling the synaptic function and structure using paired recordings from synaptically coupled neurons. *Front Synaptic Neurosci*. 2020:12.

Rall W. Branching dendritic trees and motoneuron membrane resistivity. *Exp Neurol*. 1959:1:491–527.

Rall W. Distributions of potential in cylindrical coordinates and time constants for a membrane cylinder. *Biophys J*. 1969a:9:1509–1541.

Rall W. Time constants and electrotonic length of membrane cylinders and neurons. *Biophys J*. 1969b:9:1483–1508.

Rall W. Dendritic spines, synaptic potency and neuronal plasticity. In: *Cellular mechanisms subserving changes in neuronal activity Brain Information Service*. University of California Los Angeles; 1974. pp. 13–21.

Rall W, Agmon-Snir H. 2001. Methods in neuronal modeling (2nd Edition), by C. Koch & I. Segev (eds.). *Int J Neural Syst*. 10:331–332.

Reyes A, Sakmann B. Developmental switch in the short-term modification of unitary EPSPs evoked in layer 2/3 and layer 5 pyramidal neurons of rat neocortex. *J Neurosci*. 1999:19: 3827–3835.

Richardson MJ, Silberberg G. Measurement and analysis of postsynaptic potentials using a novel voltage-deconvolution method. *J Neurophysiol*. 2008:99:1020–1031.

Rinzel J, Rall W. Transient response in a dendritic neuron model for current injected at one branch. *Biophys J*. 1974:14:759.

Sarid L, Feldmeyer D, Gidon A, Sakmann B, Segev I. Contribution of intracolumnar layer 2/3-to-layer 2/3 excitatory connections in shaping the response to whisker deflection in rat barrel cortex. *Cereb Cortex*. 2015:25:849–858.

Schiller J, Major G, Koester HJ, Schiller Y. NMDA spikes in basal dendrites of cortical pyramidal neurons. *Nature*. 2000:404: 285–289.

Schmidt ERE, Zhao HT, Park JM, Dahan JB, Rodgers CC, Hillman EMC, Polleux F. A human-specific modifier of cortical circuit connectivity and function improves behavioral performance. *Nature*. 2021:599(7886):640–644.

Seeman SC, Campagnola L, Davoudian PA, Hoggarth A, Hage TA, Bosma-Moody A, Jarsky T. Sparse recurrent excitatory connectivity in the microcircuit of the adult mouse and human cortex. *Elife*. 2018:7.

Segev I, Rall W. Computational study of an excitable dendritic spine. *J Neurophysiol*. 1988:60:499–523.

Shepherd GM. Corticostriatal connectivity and its role in disease. *Nat Rev Neurosci*. 2013:14:278–291.

Szegedi V, Paizs M, Csakvari E, Molnar G, Barzo P, Tamas G, Lamsa K. Plasticity in single axon glutamatergic connection to GABAergic

interneurons regulates complex events in the human neocortex. *PLoS Biol*. 2016:14:e2000237.

Szegedi V, Molnár G, Paizs M, Csakvari E, Barzó P, Tamás G, Lamsa K. High-precision fast-spiking basket cell discharges during complex events in the human neocortex. *eNeuro*. 2017:4(5):ENEURO.0260-17.2017.

Testa-Silva G, Verhoog MB, Goriounova NA, Loebel A, Hjorth J, Baayen JC, Mansvelder HD. Human synapses show a wide temporal window for spike-timing-dependent plasticity. *Front Synaptic Neurosci*. 2010:2:12.

Testa-Silva G, Verhoog MB, Linaro D, de Kock CP, Baayen JC, Meredith RM, Mansvelder HD. High bandwidth synaptic communication and frequency tracking in human neocortex. *PLoS Biol*. 2014:12:e1002007.

Tonnesen J, Katona G, Rozsa B, Nagerl UV. Spine neck plasticity regulates compartmentalization of synapses. *Nat Neurosci*. 2014:17: 678–685.

Tsodyks MV, Markram H. The neural code between neocortical pyramidal neurons depends on neurotransmitter release probability. *Proc Natl Acad Sci*. 1997:94:719–723.

Van Geit W, Gevaert M, Chindemi G, Rössert C, Courcol J-D, Muller EB, Markram H. BluePyOpt: leveraging open source software and cloud infrastructure to optimise model parameters in neuroscience. *Front Neuroinform*. 2016:10: 17–17.

van Pelt J, van Ooyen A, Uylings HB. Axonal and dendritic density field estimation from incomplete single-slice neuronal reconstructions. *Front Neuroanat*. 2014:8:54.

Varela F, Lachaux JP, Rodriguez E, Martinerie J. The brainweb: phase synchronization and large-scale integration. *Nat Rev Neurosci*. 2001:2:229–239.

Velmeshev D, Schirmer L, Jung D, Haeussler M, Perez Y, Mayer S, Kriegstein AR. Single-cell genomics identifies cell type-specific molecular changes in autism. *Science*. 2019:364:685–689.

Verhoog MB, Goriounova NA, Obermayer J, Stroeder J, Hjorth JJ, Testa-Silva G, Mansvelder HD. Mechanisms underlying the rules for associative plasticity at adult human neocortical synapses. *J Neurosci*. 2013:33:17197–17208.

Wang X-J. Synaptic basis of cortical persistent activity: the importance of NMDA receptors to working memory. *J Neurosci*. 1999:19: 9587–9603.

Wang XJ. Synaptic reverberation underlying mnemonic persistent activity. *Trends Neurosci*. 2001:24:455–463.

Wang X-J. Macroscopic gradients of synaptic excitation and inhibition in the neocortex. *Nat Rev Neurosci*. 2020:1–10.

Wang M, Yang Y, Wang CJ, Gamo NJ, Jin LE, Mazer JA, Arnsten AF. NMDA receptors subserve persistent neuronal firing during working memory in dorsolateral prefrontal cortex. *Neuron*. 2013:77:736–749.

Wilks DS. Frequentist statistical inference. In: Wilks DS, editors. *Statistical methods in the atmospheric sciences*. Fourth ed. Amsterdam, the Netherlands: Elsevier; 2019. pp. 143–207

Wong CH, Siah KW, Lo AW. Estimation of clinical trial success rates and related parameters. *Biostatistics (Oxford, England)*. 2019:20: 273–286.

Yakoubi R, Rollenhagen A, von Lehe M, Miller D, Walkenfort B, Hasenberg M, Lübke JH. Ultrastructural heterogeneity of layer 4 excitatory synaptic boutons in the adult human temporal lobe neocortex. *Elife*. 2019:8.

Yang D, Qi G, Ding C, Feldmeyer D. Layer 6A pyramidal cell subtypes form synaptic microcircuits with distinct functional and structural properties. *Cereb Cortex*. 2021.